Enhanced adsorption of As(V) and Mn(VII) from industrial wastewater using multi-walled carbon nanotubes and carboxylated multi-walled carbon nanotubes

T.C. Egbosiuba [a, c, e, *], A.S. Abdulkareem [a, e], A.S. Kovo [a, e], E.A. Afolabi [a], J.O. Tijani [b, e], W.D. Roos [d]

[a] Department of Chemical Engineering, Federal University of Technology, PMB.65, Minna, Niger State, Nigeria
[b] Department of Chemistry, Federal University of Technology, PMB.65, Minna, Niger State, Nigeria
[c] Department of Chemical Engineering, Chukwuemeka Odumegwu Ojukwu University, PMB 02, Uli, Anambra State, Nigeria
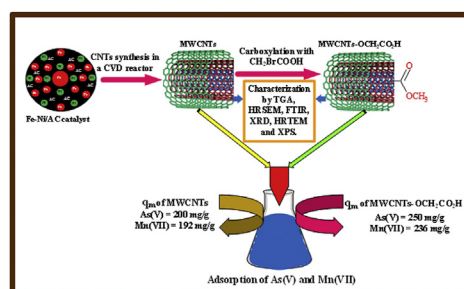[d] Department of Physics, University of the Free State, P.O. Box 339, ZA-9300, Bloemfontein, South Africa
[e] Nanotechnology Research Group, Africa Centre of Excellence for Mycotoxin and Food Safety, Federal University of Technology, P.M.B 65, Minna, Niger State, Nigeria

HIGHLIGHTS

- Preparation of bimetallic (Fe—Ni) supported activated carbon catalyst using RSM.
- MWCNTs was successfully prepared and functionalized to obtain MWCNTs-OCH$_2$CO$_2$H.
- Carboxylation enhanced the adsorption capacity of MWCNTs-OCH$_2$CO$_2$H to 250 and 238 mg/g for As(V) and Mn(VII).
- Improved adsorption by MWCNTs-OCH$_2$CO$_2$H was due to metal ions strong binding on carboxyl methoxy groups.
- MWCNTs and MWCNTs-OCH$_2$CO$_2$H significantly treated the wastewater to attain WHO standard for reuse.

GRAPHICAL ABSTRACT

ARTICLE INFO

ABSTRACT

The presence of As(V) and Mn(VII) in water beyond the permissible concentration allowed by World Health Organization (WHO) standard affects human beings, animals and the environment adversely. Hence, there is need for an efficient material to remove these potentially toxic elements from wastewater prior to discharge into water bodies. This research focused on the application of response surface method (RSM) assisted optimization of Fe—Ni/Activated carbon (AC) catalyst for the synthesis of MWCNTs. Also, the MWCNTs was carboxylated and the adsorption behaviors of both nano-adsorbents in the removal of As(V) and Mn(VII) from industrial wastewater was investigated through experimental and computational techniques. The prepared Fe—Ni/AC, MWCNTs and MWCNTs-OCH$_2$CO$_2$H were characterized using BET, TGA, FTIR, HRSEM, HRTEM, XRD and XPS. The result showed the BET surface area of Fe—Ni/AC, MWCNTs and MWCNTs-OCH$_2$CO$_2$H were obtained as 1100, 1250 and 1172 m^2/g, respectively. Due to the enhanced

* Corresponding author. Department of Chemical Engineering, Chukwuemeka Odumegwu Ojukwu University, PMB 02, Uli, Anambra State, Nigeria.
E-mail addresses: ct.egbosiuba@coou.edu.ng, egbosiubachinedu@gmail.com (T.C. Egbosiuba).

impact of carboxylation, the adsorption capacity of As(V) and Mn(VII) removal increased from 200 to 192 mg/g for MWCNTs to 250 and 298 mg/g for MWCNTs-OCH$_2$CO$_2$H. The isotherm and kinetic models were best fitted by Langmuir and pseudo-second order kinetics, while the thermodynamic investigation found that the adsorption process was endothermic, spontaneous and chemisorptions controlled. The regeneration potential of MWCNTs and MWCNTs-OCH$_2$CO$_2$H after six repeated applications revealed good stability of adsorption efficiency. The study demonstrated optimization importance of Fe−Ni/AC catalyst design for MWCNTs adsorbents and the potentials of utilizing both MWCNTs and MWCNTs-OCH$_2$CO$_2$H in the removal of selected heavy metals from water and soil.

1. Introduction

Wastewater generated from chemical industries constitutes one of the main sources of contamination of the environment and water sources (Joseph et al., 2019). Hazardous metal ions like Arsenic (As), Manganese (Mn), Nickel (Ni), Chromium (Cr), Cadmium (Cd), Lead (Pb), Iron (Fe), Copper (Cu), Zinc (Zn) and Mercury (Hg) are one of the key pollutants contained in wastewater from chemical industries (Lee et al., 2017). The characteristic attribute of these heavy metals is non-biodegradability, prolonged accumulation, high toxicity and mobility (Oh et al., 2019). The long-term exposure of human beings to As(V) and Mn(VII) may cause various adverse health effects such as cancer, neurotoxicity, damage of nervous system, birth defects, manganism and liver damage (Yadav et al., 2019). For instance, maximum permissible concentrations of arsenic and manganese for a safe water for drinking purposes are 0.2 and 0.5 mg/L, respectively (US EPA, 2012). Therefore, it is important to treat industrial wastewater to remove heavy metals prior to reuse or discharge into the water bodies.

Meanwhile, various treatment technologies have been employed such as ion exchange (Zhao et al., 2019a, 2019b), chemical oxidation (Oh et al., 2020), filtration (Bhateria and Singh, 2019), membrane technology (Byun et al., 2019), coagulation (Bora and Dutta, 2019), flocculation and electro-coagulation process to treat complex industrial wastewater (Fu et al., 2019). These techniques have certain limitations such as high cost of reagents, generation of toxic sludge, occupation of space, high energy requirements amongst others (Gholipour et al., 2020). Conversely, adsorption technology shows exceptional characteristics such as simplicity in design, cost effectiveness, environmental friendliness and high removal efficiency especially when heavy metals concentration in wastewater ranges from 1 to 100 mg/L (Yang et al., 2019a, 2019b). For this purpose, adsorbents like activated carbon (Roh et al., 2018), clays (Pietrelli et al., 2019), metal oxide/hydroxide (Siddiqui and Chaudhry, 2017) and nanomaterials have been used by different researchers to sequester heavy metals from wastewater (Siddiqui et al., 2019). Among these adsorbents, nanomaterials such as carbon nanotubes (Xu et al., 2018) have been developed to remove arsenic and manganese from wastewater.

Carbon nanotubes have gained extensive attention over other nanoparticles due to their excellent structure and physical properties that influences the chemical, mechanical, optical, electrical, thermal and adsorptive properties of CNTs (Veksha et al., 2020). The techniques for the synthesis of CNTs includes arc-discharge (Yatom et al., 2017), chemical vapor deposition (CVD) (Ahamed et al., 2019) and laser ablation (Yang et al., 2019a, 2019b). Both arc discharge and laser ablation synthesis routes are batch processes characterized by high synthesis temperature, high design cost, high energy requirement, low CNTs yield, low CNTs selectivity, design difficulty and growth variables control (Bankole et al., 2018a, 2018b). On the other hand, CVD method is a continuous process with low synthesis temperature, low energy requirements, high metal catalysts influence, high CNTs selectivity, availability of carbon source, ease of design and growth variables control to obtain high CNTs yield (Chen et al., 2020; Malekimoghadam, 2018).

Various process parameters such as catalyst, carbon source, carrier gas, growth temperature and time have been identified to exert great influence on the CNTs yield and quality (Shukrullah et al., 2016). Among all the growth parameters, catalyst has been widely proved to perform key functions during CNTs growth (Moo et al., 2019). Although, transition metals such as Fe, Ni, Co, Mo, Mn, Cu, Pt can be impregnated on the support material (kaolin, zeolite, CaCO$_3$, MgO, Al$_2$O$_3$) for the growth of carbon nanotubes, studies have shown that the combination of transition metals (bimetallic catalysts) enhances the synthesis of MWCNTs of high yield and quality (Nahil et al., 2015). Furthermore, it is required that catalysts for carbon nanotubes synthesis undergo high-temperature post-treatment process like calcinations to remove residual elements (chloride, nitrate or sulfide) and water at the temperature range 350−600 °C, and eventually form active metals (Nadar et al., 2018). Due to catalyst deactivation caused by the oxidic catalyst supports and post-calcination treatment process, there is need for alternative supports that is effective in the dispersion and stabilization of catalyst particles after the deposition of the catalysts under less intense post-thermal treatment (Luo et al., 2018).

In the recent times, researchers have identified non-oxidic catalyst supports such as activated carbon (AC) for CNTs growth due to the controlled dispersion of metal particles and the non-formation of inactive materials like carbonates, aluminates and silicates (Almkhelfe et al., 2018; Pérez-Mayoral et al., 2016). Similarly, AC is largely considered due to its resistance to acidic and basic environments, low cost, mechanical and thermal stability and porosity control (Maharjan et al., 2019). Other properties possessed by AC include: flexibility of definite interactions of metal-support that enhances the activity and selectivity, and above all they are very cheap compared to previously utilized supports such as carbonate, alumina and silica (Luo et al., 2018; Pérez-Mayoral et al., 2016).

The optimization of Fe−Ni catalyst preparation on AC support at different temperature, time, stirring speed and mass of catalyst using response surface method (RSM) stimulates the growth of CNTs. RSM is an important optimization technique that examines the interaction of two or more process parameters. Factorial design have been used to optimize Fe−Co catalyst preparation on CaCO$_3$ support for MWCNTs synthesis (Bankole et al., 2018a, 2018b). Aliyu et al. (2017) also reported the synthesis of MWCNTs on Fe−Ni catalyst prepared on kaolin support. The influence of Fe−Ni catalysts on different Al$_2$O$_3$ supports was examined for the synthesis of CNTs from waste plastics (Yao et al., 2018). Previous study on the synthesis of CNTs from plastics using metallic nickel catalysts (Jia et al., 2020) revealed that the activities of nickel catalysts were highly dependent on the interaction of metal support. The

Table 1
(a) Actual and coded values of RSM optimization and (b) detailed experimental run for Fe–Ni/AC catalyst preparation.

Process Parameters	Code	Coded Values				
		$-\alpha$	-1	0	$+1$	$+\alpha$
a.						
Mass of AC support (g)	A	4	6	8	10	12
Stirring speed (rpm)	C	100	250	400	550	700
Pre-calcination temperature (^{o}C)	D	105	110	115	120	125
Pre-calcination time (h)	B	6	8	10	12	14

b.				
Run	Mass of AC support (g)	Stirring speed (rpm)	Pre-calcination temperature (^{o}C)	Pre-calcination time (h)
1(FT)	10	550	120	12
2(FT)	10	550	120	8
3(FT)	10	550	110	12
4(FT)	10	550	110	8
5(FT)	10	250	120	12
6(FT)	10	250	120	8
7(FT)	10	250	110	12
8(FT)	10	250	110	8
9(FT)	6	550	120	12
10(FT)	6	550	120	8
11(FT)	6	550	110	12
12(FT)	6	550	110	8
13(FT)	6	250	120	12
14(FT)	6	250	120	8
15(FT)	6	250	110	12
16(FT)	6	250	110	8
17(CP)	8	400	115	10
18(CP)	8	400	115	10
19(CP)	8	400	115	10
20(CP)	8	400	115	10
21(CP)	8	400	115	10
22(CP)	8	400	115	10
23 (AC)	12	400	115	10
24 (AC)	4	400	115	10
25 (AC)	8	700	115	10
26 (AC)	8	100	115	10
27 (AC)	8	400	125	10
28 (AC)	8	400	105	10
29 (AC)	8	400	115	14
30 (AC)	8	400	115	6

FT=Factorial, AP = Axial Point and CP=Centre Point.

synthesis of CNTs using Fe–Ni catalyst on rice straw support was demonstrated by (Fathy, 2017). In another study, Sivakumar et al. (2011) reported that CNTs was synthesized on AC supported Fe–Ni catalyst, but the authors did not optimize the preparation of the Fe–Ni/AC to enhance the surface properties. To the best of our knowledge, no previous study has investigated the optimization of the preparation of Fe–Ni on AC support using central composite design (CCD) adapted RSM. In addition, no researcher has reported the adsorption potentials of carboxylated MWCNTs synthesized from Fe–Ni/AC catalysts for As and Mn uptake from chemical industrial wastewater.

This paper reports for the first time the development of Fe–Ni/AC catalyst using RSM. The obtained catalyst at the optimum conditions was calcined and used for the synthesis of MWCNTs. The as-synthesized MWCNTs were purified by acids followed by carboxylation with $CH_2BrCOOH$. The MWCNTs and MWCNTs-OCH_2CO_2H nano adsorbent were characterized and investigated for the sequestration of As(V) and Mn(VII) from chemical industrial wastewater. The adsorption isotherms, kinetics and thermodynamics parameters were evaluated. The successful utilization of AC as bimetallic (Fe–Ni) catalyst support for MWCNTs growth represents a viable innovative alternative to the previously used support materials and a crystal improvement on the current methods, yielding high quality MWCNTs.

2. Materials and methods

2.1. Materials

All chemicals used in this study were Analytical Grade (AR). The high purity iron (III) trioxonitrate (V) nonahydrate ($Fe(NO_3)_3 \cdot 9H_2O$), nickel (II) trioxonitrate (V) hexahydrate ($Ni(NO_3)_2 \cdot 6H_2O$), tetraoxosulphate (VI) acid (H_2SO_4), sodium hydroxide (NaOH) and bromoacetic acid ($CH_2BrCOOH$) with percentage purity (95–99.9%) were purchased from Sigma Aldrich Chemicals and used without further purification. The argon, acetylene and nitrogen gases were of high percentage purity (>98%) and purchased from British Oxygen Company (BOC Gases) Lagos, Nigeria. The chemical industrial wastewater was collected from industrial layout Nnewi, Nigeria. Activated carbon (AC) was prepared via ultrasonic enhanced influence on the surface area of AC from Empty Fruit Bunch (EFB) as reported in our previous study (Egbosiuba et al., 2019).

2.2. Optimization of Fe–Ni/AC catalyst preparation

RSM was utilized to study mass of support, stirring speed, drying temperature and drying time influence on Fe–Ni/AC catalyst yield. The parameters values for catalyst preparation were obtained from preliminary investigation trial runs using literature data. The

considered actual and coded preparation factors are presented in Table 1a.

A known weight (4.0 g) and (3.0 g) of $Fe(NO_3)_3 \cdot 9H_2O$ and $Ni(NO_3)_2 \cdot 6H_2O$ was weighed and made to dissolve in distilled water (50 cm^3). 10 g of the AC support was added to the solution and stirred continuously at stirring speed of 550 rpm for 10 min. The obtained slurry was oven dried at 120 °C for 12 h. The sample was cooled to room temperature and ground with mortar to avoid agglomeration. The catalyst samples were screened using 150 μm sieve, weighed and recorded. The yield of the dried catalyst was calculated using Eq. (1) (Bankole et al., 2018a, 2018b). The experimental runs of the applied conditions presented in Table 1b were carried out using the same procedure.

$$\text{Yield}_{\text{Dried}}(\%) = \frac{\text{Mass after oven drying}}{\text{Initial mass of mixture}} \times 100\ \% \qquad 1$$

The obtained optimum yield was subjected to calcinations at 350 and 400 °C for 4 and 6 h respectively to remove residual nitrates and moisture in the samples. Brunauer-Emett-Teller (BET) technique was used to determine the calcined Fe–Ni/AC catalyst surface area. Also, the yield of Fe–Ni catalyst after calcinations was calculated using Eq. (2) (Bankole et al., 2018a, 2018b).

$$\text{Yield}_{\text{Calcined}}(\%) = \frac{\text{Mass after calcination}}{\text{Mass after oven drying}} \times 100\ \% \qquad 2$$

For the statistical analysis of the results, all the experiments were conducted in triplicate (n = 3). The influence of process variables on the yield of Fe–Ni/AC catalysts aided the conduct of Analysis of Variance (ANOVA) to show the main and combined effects of the factors considered as indicated in the empirical models in order to validate yield dependence on these parameters.

2.3. Synthesis of MWCNTs

The calcined Fe–Ni/AC catalyst (5 g) was weighed and put into a ceramic boat positioned at the quartz tube centre of the CVD furnace. The purging of the system of air carried out through the flow of argon gas (30 mL/min) over the Fe–Ni/AC at the heating rate of 10 °C/min. At the temperature of 750 °C, argon gas flow rate was adjusted to 250 mL/min and acetylene gas flow rate was set at 200 mL/min for 60 min. Thereafter, the furnace was allowed to cool to room temperature and the ceramic boat withdrawn for weighing and recording of the produced CNTs yield. The percentage yield of CNTs was determined using the mathematical expression shown in Eq. (3) (Bankole et al., 2018a, 2018b).

$$\text{CNTs Yield}\ (\%) = \frac{M_{\text{total}} - M_{\text{catalyst}}}{M_{\text{catalyst}}} \times 100\ \% \qquad (3)$$

where M_{total} is the total mass of the Fe–Ni/AC catalyst and CNTs after CVD reaction process while M_{catalyst} is the initial mass of Fe–Ni/AC catalyst.

2.4. Functionalization of MWCNTs

The produced carbon nanotubes were purified by acid treatment technique (HNO_3 and H_2SO_4 mixture) for the removal of residual iron, nickel, amorphous carbon and other impurities introduced into the catalyst samples during synthesis. MWCNTs (5 g) was sonicated in distilled water (100 mL) and NaOH (8 g) for 3 h $CH_2BrCOOH$ (10 g) was added and the resulting mixture sonicated for 3 h. Afterwards, distilled water was used to wash the mixture to achieve a pH of 7. Subsequently, the mixture was filtered and oven dried at 120 °C for 10 h to obtain MWCNTs-OCH_2CO_2H.

2.5. Characterization

The morphology, functional groups, surface area and thermal stability of Fe–Ni/AC catalyst, MWCNTs and MWCNTs-OCH_2CO_2H were characterized by high resolution scanning electron microscopy (HRSEM, Zeiss Auriga), Fourier-transform infrared (FT-IR, Frontier FT-IR, PerkinElmer, UK), Brunauer-Emett-Teller (BET, NOVA4200e, Quantachrome UK) and thermogravimetric analysis (TGA, PerkinElmer, UK). The microstructures, phase structures, oxidation states and functional groups of MWCNTs-OCH_2CO_2H were also characterized by high resolution transmission electron microscopy (HRTEM, Zeiss Auriga), X-ray diffraction (XRD, 6000, Shimadzu Scientific) and X-ray photoelectron spectrometry (XPS, PHI 5400 instrument, USA). A pH meter (Eutech Instruments) was used to determine the charge densities of the solution as the charge on the surface of MWCNTs and MWCNTs-OCH_2CO_2H was adjusted between 2 and 8 using 0.1 M of H_2SO_4 and NaOH until the charge density became zero. The point at which the pH of the solution became zero was noted as the point of zero charge (PZC).

2.6. Metal analysis

Prior to the supernatants preparation, the concentration of As(V) and Mn(VII) in the raw chemical industry wastewater was analyzed by atomic adsorption spectrophotometer (AAS, PG 990, PG Instruments, UK). The preparation of the supernatants in the adsorption studies was carried out using water bath (SB25-12DT, Scientz). The supernatants were filtered prior to analysis for the As(V) and Mn (VII) concentration by AAS method.

2.7. Batch adsorption studies

The selected heavy metal (HM) ions (As(V) and Mn(VII)) adsorption on MWCNTs and MWCNTs-OCH_2CO_2H nano-adsorbent was conducted through batch adsorption using wastewater from chemical industries. The calculation of the adsorption percentage and adsorption capacity (q_e) were carried out using Eqs. (4) and (5), respectively (Huang et al., 2019).

$$\%\ \text{Removal} = \frac{C_0 - C_{e,t}}{C_0} \times 100 \qquad 4$$

$$q_e = \frac{(C_0 - C_e)V}{m} \qquad 5$$

where q_e (mg/g) indicates the adsorption capacity of HM adsorbed per gram of the adsorbent at equilibrium, C_0 (mg/L) and C_e (mg/L) denotes the initial and equilibrium concentrations of HM, m (mg) refers to the adsorbent mass used during the adsorption process and V (L) is the adsorbate solution volume. The influence of solution contact time, adsorbent dosage, temperature and pH were investigated and described as follows:

To determine contact time influence for As(V) and Mn(VII) adsorption on MWCNTs and MWCNTs-OCH_2CO_2H, 20 mg of nano-adsorbent was added to 100 cm^3 of chemical industry wastewater in a conical flask of 250 cm^3. The mixtures were corked and placed in the water bath at 40 °C and a constant pH (5) for stirring at various contact time (5, 10, 20, 30, 40, 60, 120 and 180 min).

For the investigation of influence of adsorbent dosage for As(V) and Mn(VII) adsorption on MWCNTs and MWCNTs-OCH_2CO_2H, different amounts of nano-adsorbent (10, 20, 30, 40, 50 and 60 mg) was mixed with 100 cm^3 of chemical industry wastewater in a conical flask of 250 cm^3. The mixtures were corked and stirred in a water bath at 40 °C and pH (5) for 60 min (equilibrium time).

The adsorption of As(V) and Mn(VII) onto MWCNTs and

MWCNTs-OCH$_2$CO$_2$H was evaluated at various temperatures (25, 30, 35, 40 and 50 °C) by mixing 30 mg of the nano-adsorbent into a 250 cm^3 conical flask with 100 cm^3 of chemical industry wastewater maintained at a pH of 5. The mixtures were corked and stirred in a water bath to attain an equilibrium time of 60 min.

The solution pH influence on the uptake of As (V) and Mn(VII) by MWCNTs and MWCNTs-OCH$_2$CO$_2$H was investigated. The chemical industry wastewater initial pH was adjusted to 2−7 by either 0.1 M NaOH or 0.1 M H$_2$SO$_4$. At each pH, 30 mg each of MWCNTs and MWCNTs-OCH$_2$CO$_2$H was mixed with 100 cm^3 of the chemical industry wastewater in a conical flask of 250 cm^3. The corked mixtures were stirred in a water bath at 50 °C for a period of 60 min.

Thereafter, the mixtures obtained at each contact time, adsorbent dosage, temperature and solution pH were filtered using Whatmann grade 1 filter paper and the supernatants were collected to determine the equilibrium concentration (C$_e$) of As(V) and Mn(VII) by AAS method. The C$_e$ was applied to evaluate the equilibrium adsorption capacity (q$_e$).

2.8. Ionic strength

For ionic strength evaluation, 30 mg each of MWCNTs and MWCNTs-OCH$_2$CO$_2$H was also mixed with 100 cm^3 of the chemical industry wastewater in a 250 cm^3 conical flask using KCl and NaCl in the concentration range of 0.1−1.0 mol/L. at the temperature (50 °C), adsorbent dosage (30 mg) and solution pH (8). The corked mixtures were further stirred for 60 min and thereafter filtered using Whatmann grade 1 filter paper. The filtrate was analyzed for As(V) and Mn(VII) using AAS.

2.9. Reusability investigation

Regeneration potential of MWCNTs and MWCNTs-OCH$_2$CO$_2$H was evaluated using H$_2$SO$_4$ (0.1 M) as a washing solution after the adsorption process. Specifically, 30 mg of As (V) and Mn (VII) adsorbed MWCNTs-OCH$_2$CO$_2$H was added to 100 cm^3 of the washing solution and the mixture was shaken for 3 h. Thereafter, the nano-adsorbent was separated by filtration using 0.2 mm filter paper and washed severally. The reusability of the nano-adsorbent was repeated for 5 cycles to examine the regeneration capacity of MWCNTs and MWCNTs-OCH$_2$CO$_2$H. The re-adsorption ability was calculated as follows (Zhao et al., 2019a, 2019b);

$$\frac{q_{e,n}}{q_{e,0}} \times 100\% \qquad\qquad 6$$

where q$_{e,n}$ describes the adsorption capacity of the nano-adsorbent after n cycles, while q$_{e,0}$ refers to the capacity without regeneration.

2.10. Computational analysis

2.10.1. Adsorption kinetics

The capacity of adsorption (qt) was determined and analyzed by pseudo-first-order, pseudo-second-order, Elovich and intra-particle diffusion (Ho, 2006; Martinez−Vargas et al., 2018) for the experimental data evaluation. The linear fitting technique from Origin software (Origin Pro 9.0, Origin Lab Corporation) was applied to analyze the experimental adsorption rate data.

The pseudo first order model is expressed as follows (Ho, 2006):

$$In\,(q_e - q_t) = In\,q_e - k_1 t \qquad\qquad 7$$

The pseudo-second-order model is represented as follows (Ho, 2006):

$$\frac{t}{q_t} = \frac{1}{k_2 q_e^2} + \frac{t}{q_e} \qquad\qquad 8$$

The Elovich model is mathematically presented as follows (Kazak et al., 2018):

$$q_t = \left(\frac{1}{b}\right)In\,(ab) + \left(\frac{1}{b}\right)In\,t \qquad\qquad 9$$

The intraparticle diffusion model representation is shown as follows (Martinez−Vargas et al., 2018):

$$q_t = k_{int} t^{1/2} + C \qquad\qquad 10$$

where q$_e$ (mg/g) denotes the adsorbed quantity of As(V) and Mn (VII) at equilibrium, q$_t$ (mg/g) indicates the As(V) and Mn(VII) adsorbed quantity at time t (min), k$_1$ (min^{-1}), k$_2$ (mg/g.min), k$_{int}$ (mg/g.min$^{0.5}$) and α (mg/g.min) refers to the constant rates for pseudo-first order, pseudo-second order and intraparticle diffusion models. The a in the Elovich kinetic model refers to the initial adsorption rate (g/mg·min^2), while b is the extent of surface coverage coefficient (mg/g·min). In intraparticle diffusion model, C (mg/g) is the constant for the thickness of boundary layer.

2.10.2. Adsorption isotherm

The equilibrium concentration (C$_e$) was applied to calculate the equilibrium capacity of adsorption (q$_e$). Adsorption isotherm was evaluated by fitting the experimental data to the linearized forms of Langmuir, Freundlich, Temkin and Dubinin-Radushkevich (D-R) isotherm (Langmuir, 1918; Siyal et al., 2019; Dubinin, 1969).

The Langmuir isotherm model is denoted as follows (Langmuir, 1918):

$$\frac{C_e}{q_e} = \frac{1}{K_L q_m} + \frac{C_e}{q_m} \qquad\qquad 11$$

Freundlich isotherm model equation is described as follows (Siyal et al., 2019):

$$In q_e = In\,K_F + \frac{1}{n_F} In C_e \qquad\qquad 12$$

Temkin isotherm model equation is presented as follows (Zhao et al., 2019a, 2019b):

$$q_e = \frac{RT}{b_T} In A_T + \left(\frac{RT}{b_T}\right) In C_e \qquad\qquad 13$$

D-R isotherm model is represented as follows (Dubinin, 1969):

$$In\,q_e = In q_s - k_{ad} n^2 \qquad\qquad 14$$

where q$_e$ (mg/g) is the adsorption capacity at equilibrium for As(V) and Mn (VII), q$_m$(mg/g) refers to the maximum adsorption capacity for monolayer coverage on the nano-adsorbent surface, C$_e$ (mg/L) indicates the As(V) and Mn(VII) concentration at equilibrium. k$_L$ (L.mg^{-1}) is the Langmuir equilibrium adsorption constant. K$_F$ (mg/g) and n$_F$ = the Freundlich adsorption isotherm constant denoting the adsorption capacity of the nano-adsorbent and the heterogeneity of adsorption process respectively. b$_T$ (kJ/mol) and A$_T$ (L/g) are the Temkin constants that are related to the heat of adsorption and maximum binding energy. T is the temperature (°C), while R (8.314 J/mol.K) = universal gas constant. The constants, q$_{ad}$ and q$_s$ are related to the mean free energy of adsorption and the monolayer saturation of D-R capacity of adsorption. Also, n is a Polyani potential.

2.10.3. Adsorption thermodynamics

The nature of the adsorption of As(V) and Mn(VII) onto MWCNTs and MWCNTs-OCH$_2$CO$_2$H was determined by the determination of the thermodynamic parameters such as Gibbs free energy ($\Delta G°$), enthalpy ($\Delta H°$), entropy ($\Delta S°$) and activation energy (E_a). The Van't Hoff expression was utilized to evaluate the Gibbs energy change (ΔG, kJ/mol) shown in Eqs. (15) and (16) respectively (Huang et al., 2019);

$$\Delta G° = \Delta H° - T\Delta S° \qquad 15$$

$$\ln \frac{q_e}{C_e} = - \frac{\Delta H°}{RT} + \frac{\Delta S°}{R} \qquad 16$$

where $\Delta H°$ (J mol^{-1}) and $\Delta S°$ (J K^{-1} mol^{-1}) represent the standard enthalpy and entropy change. R is the universal gas constant (8.314 JK^{-1} mol^{-1}), while T denotes temperature (K), $\Delta H°$ (kJ mol^{-1}) and $\Delta S°$ (kJ K^{-1} mol^{-1}) were determined from the slope and intercept of a linear plot of $\ln \frac{q_e}{C_e}$ against $\frac{1}{T}$ respectively.

2.10.4. Error analysis

All the experiments were carried out in triplicate to enhance validation of the results. Statistical error analysis such as linear determination coefficient (R^2), the non-linear Chi-square test (χ^2) and the sum of square error (SSE) was used to evaluate the fitness of the isotherm and kinetic model to the experimental data. The mathematical expressions are represented in Eqs. (17) and (18) as follows (Mouni et al., 2018):

$$X^2 = \sum \left(q_{e, \exp} - q_{e, \mathrm{cal}} \right)^2 \Big/ q_{e, \mathrm{cal}} \qquad 17$$

$$SSE = \sum \left(q_{e, \exp} - q_{e, \mathrm{cal}} \right)^2 \qquad 18$$

where $q_{e, \exp}$ (mg/g) and $q_{e, \mathrm{cal}}$ (mg/g) describe the experimental and calculated equilibrium capacity respectively. Small values of χ^2 and SSE, indicates the similarity to the experimental data, while higher values describes that the model data differs with the experimental data.

3. Results and discussion

3.1. Optimization of Fe−Ni/AC catalyst

RSM optimization technique was utilized to study the effects of mass of AC support, stirring speed, pre-calcination temperature and pre-calcination time on the yield of supported bimetallic Fe−Ni catalyst on AC. The drying of the catalysts was also employed to achieve successful dispersion of Fe and Ni metals on AC support.

3.1.1. Effect of pre-calcination temperature

Pre-calcination temperature was investigated on the preparation of Fe−Ni/AC catalyst and the result is presented in Table E1 (Supplementary data). It was observed that at the pre-calcination temperatures of 105, 110 and 115 °C, the yields of Fe−Ni/AC were 80.65, 85.0 and 92.5%, respectively. However, with further increase in temperature from 120 to 125 °C, the yield of Fe−Ni/AC catalyst reduced to 85.40 and 76.20%, respectively. As shown in Table E1 the optimum yield of Fe−Ni/AC (92.5%) was achieved at the pre-calcination temperature (115 °C), pre-calcination time (10 h), stirring speed of (400 rpm) and mass of AC (8 g). The increasing trend of catalyst yield from 105 to 115 °C could be attributed to the improved diffusion of metallic particles onto the surface of the substrate. Furthermore, as the temperature was increased to 120 °C

and 125 °C, significant reduction of Fe−Ni/AC catalysts yield from 85.4% to 76.2% was observed and was linked to loss of entrapped liquid in the pores through diffusion.

3.1.2. Effect of pre-calcination time

The influence of pre-calcination time on the yield of Fe−Ni/AC catalyst yield was investigated and the result is presented in Table E1. According to Table 2, it was noticed that at the pre-calcination time of 6, 8 and 10 h, the obtained catalyst yields were 82.1, 85.0 and 92.5% yield respectively. As the pre-calcination time was further increased to 12 and 14 h, the catalyst yield reduced to 85.4 and 81.5%, respectively. The increasing yield of catalyst at the pre-calcination time of 6−10 h may be ascribed to the deposition and enhanced diffusion of metallic (iron and nickel) components on the porous surface of the AC. The decrease in Fe−Ni/AC catalyst yield at higher pre-calcination time may be due to the diffusion of the entrapped liquid in the solid pores (Nadar et al., 2018). The precipitation of unabsorbed solute from the blocked or entrapped liquid in the pores of the solid during the process of pre-calcination may also be responsible for the reduced yield (Jiang et al., 2018).

3.1.3. Effect of stirring speed

The effect of stirring speed on Fe−Ni/AC catalyst yield was studied and the result presented in Table E1. The result indicated that 77.5, 82.5 and 92.5% yield of Fe−Ni/AC catalyst was obtained at the stirring speed of 100, 250 and 400 rpm respectively. Further increment in the stirring speed to 550 and 700 rpm, caused reduction in the yield to 85.4 and 82.8%. As noticed in Table E1, maximum Fe−Ni/AC catalyst yield of 92.5% was obtained using 400 rpm stirring speed. The increment in the Fe−Ni/AC catalyst yield with increase in stirring speed may be attributed to the high adsorption rate of solute which enhanced dispersion of metallic particles onto the support during wet impregnation process (Jiang et al., 2018). On the other hand, the reduction in Fe−Ni/AC catalyst yield above the stirring speed of 400 rpm could be linked to the diffusion of moisture during pre-calcination.

3.1.4. Effect of mass of AC

Table E1 shows the yield of Fe−Ni/AC catalyst obtained from the variation of mass of AC. As shown in Table E1, Fe−Ni/AC catalyst yield of 75.1, 83.7 and 92.5% was obtained using 4, 6 and 8 g of AC. Conversely, further increase in the mass of AC to 10 and 12 g, resulted to the decrease in Fe−Ni/AC catalyst yield to 85.4 and 85.0%, respectively. As stated in Table 2, maximum Fe−Ni/AC catalyst yield of 92.5% was obtained using 8 g of AC. The enhanced catalyst yield with increasing mass of AC may be attributable to improved deposition and diffusion of metal components to the AC porous surface. The decrease in catalyst yield using higher amount of AC may be due to the availability of more AC during impregnation than diffusion rate during drying process, thereby causing decrease in yield at equilibrium between the solute adsorption and liquid diffusion.

3.1.5. Post-calcinations of Fe−Ni/AC catalyst

Post-calcination of the Fe−Ni/AC catalyst was carried out to remove the residual moisture and nitrates. The influence of post-calcination temperature and post-calcination time on the surface area of Fe−Ni/AC catalyst was investigated using the obtained optimum yield (92.5%) at pre-calcination temperature (115 °C), pre-calcination time (10 h), stirring speed (400 rpm) and mass of AC support (10 g) (Table E1). During post-calcination, the transformation of iron (III) nitrate nonahydrate and nickel (II) nitrate hexahydrate to hematite (Fe$_2$O$_3$) and nickel oxide (NiO) may occur between temperature of 250 and 300 °C respectively (Nadar et al.,

Table 2
Isotherm models calculated parameters for As(V) and Mn(VII) adsorption onto MWCNTs and MWCNTs-OCH$_2$CO$_2$H.

Isotherm	Parameters	MWCNTs		MWCNTs-OCH$_2$CO$_2$H	
		As(V)	Mn(VII)	As(V)	Mn(VII)
Langmuir	q_m (mg/g)	200 ± 2.0	192 ± 2.2	250 ± 2.1	238 ± 2.3
	K_L (L.min^{-1})	1.12 ± 0.041	0.84 ± 0.035	1.29 ± 0.045	0.96 ± 0.042
	R_L	0.014 ± 0.006	0.015 ± 0.003	0.008 ± 0.005	0.011 ± 0.004
	R^2	0.999	0.999	0.999	0.999
	SSE	0.029	0.001	0.008	0.081
	X^2	0.062	0.000	0.010	0.056
Freundlich	$1/n_F$	0.121 ± 0.012	0.144 ± 0.014	0.101 ± 0.011	0.124 ± 0.013
	n_F	8.244 ± 0.080	6.925 ± 0.071	9.950 ± 0.084	8.071 ± 0.090
	K_F (mg/g)	289.668 ± 2.601	305.141 ± 2.711	341.036 ± 2.598	357.108 ± 2.600
	R^2	0.991	0.995	0.980	0.989
	SSE	0.537	0.304	0.263	1.599
	X^2	0.112	0.184	0.203	0.180
Temkin	b_T (kJ/mol)	−761.06 ± 0.002	−651.780 ± 0.018	−905.770 ± 0.015	−752.02 ± 0.001
	A_T (L/g)	3.2 × 10^{-5}±0.001	10.3 × 10^{-5}±0.002	5.7 × 10^{-5}±0.002	3.1 × 10^{-5}±0.003
	R^2	0.996	0.996	0.984	0.984
	SSE	0.269	0.720	0.423	0.325
	X^2	0.102	0.910	0.250	0.141
D-R	K_{ad}	8 × 10^{-6}±0.030	2.0 × 10^{-6}±0.025	1.0 × 10^{-6}±0.040	5 × 10^{-5}±0.030
	q_s	210.440 ± 2.200	204.078 ± 2.150	261.256 ± 2.200	250.811 ± 2.100
	R^2	0.941	0.962	0.888	0.906
	SSE	12.142	12.216	14.916	18.728
	X^2	2.802	2.925	3.407	5.594

2018).

At the post-calcination temperature (350 °C) and holding time (4 h), the BET surface area for the catalyst was 820 m^2/g, while post-calcination of the same sample at 400 °C for 4 h had a BET surface area of 900 m^2/g. In addition, BET surface area of 880 m^2/g was obtained at the post-calcination temperature and time of 350 °C and 6 h. Again, at 400 °C for 6 h, the maximum BET surface area of 1100 m^2/g was obtained. It can be seen that at different post-calcinations temperature and holding time, the surface area of the catalyst increased due to the decomposition of the metallic salts to their respective metal oxides. Sivakumar et al. (2011) reported the decomposition of iron (III) nitrate nonahydrate and nickel (II) nitrate hexahydrate to Fe$_2$O$_3$ and NiO at 350 °C.

3.1.6. Statistical analysis of Fe−Ni/AC catalyst synthesis with respect to yield

The interactive effects of pre-calcination temperature, pre-calcination time, stirring speed and mass of AC support on the yield of Fe−Ni/AC catalyst were analyzed using Central composite design (CCD) adapted from Response surface method (RSM). The result of the Analysis of variance (ANOVA) of Fe−Ni/AC catalyst yield is presented in Table E2. As shown in Table E2, the model F-value of 84.39 from ANOVA for bimetallic Fe−Ni/AC catalyst is an indication of a significant model. Furthermore, Table E2 revealed that mass of support with the highest F-value (116.19) had the greatest effect on the yield of Fe−Ni/AC catalyst, followed by stirring speed, drying temperature, and drying time with the F-values of 36.31, 23.05 and 1.62 respectively. Among the interaction of the preparation parameters, CD with F-value of 43.76 exhibited high influence on the yield of Fe−Ni/AC. Also, the F-value of 36.33 and 35.62 obtained for the interaction of AB and AD indicated an improvement in the catalyst yield compared with the F-values of 5.67, 4.61 and 1.91 achieved for the interaction of BC, AC and BD.

Additionally, quadratic function F-values of 404.84 and 310.41 demonstrated increased impact of drying temperature and mass of support on the yield of Fe−Ni/AC, followed by stirring speed and drying time with the F-values of 305.01 and 222.72 respectively. Similarly, it was found that the operating variables exhibited substantial effects on the yield of Fe−Ni/AC catalyst due to lack of fit F-value of 1.69 which denotes insignificance relative to the pure error.

Previous researchers opined that non-significant lack of fit validates the fitness of the model (Nadar et al., 2018). The ANOVA result reveals the fitting of the experimental data to the proposed model and validates the influence of the independent variables on the yield of Fe−Ni/AC catalyst. The final equation with respect to the actual value is given in Eq. (19) as.

Fe−Ni/AC Yield = 91.6 + 1.871A + 1.046B - 0.833C - 0.221D + 1.281AB + 0.456AC + 1.269AD - 0.506BC - 0.294BD + 1.406CD - 2.860 A^2 - 2.835 B^2 - 3.267C^2 - 2.423D^2 .(19)

The developed model (Eq. (19)) describes the relationship between the preparation parameters on the yield of Fe−Ni/AC.

3.2. Characterization of Fe−Ni/AC catalyst

The results of the thermal behavior of the pre-calcined and post-calcined bimetallic Fe−Ni/AC catalyst are presented in Fig. C1a (Supplementary data). It is apparent from Fig. C1a that pre-calcined and post-calcined Fe−Ni/AC catalyst shows clear increase in weight loss with increasing temperature. The stages of weight loss in the Fe−Ni/AC catalyst thermogram were identified at the temperatures range of 100 °C - 300 °C, 300 °C - 400 °C and 400 °C - 650 °C respectively.

It is evident from the result that the loss of absorbed moisture on both the pre-calcined and post-calcined Fe−Ni/AC catalyst was responsible for the weight loss before 100 °C. The thermogram curve observed at the temperature of 100 °C - 300 °C depict the removal of crystal water of the nitrates and the elimination of volatile products. In addition, the rapid decomposition which occurred at the temperature of 300°C-500 °C indicates the oxidative decomposition of iron and nickel nitrates mixture. The percentage weight loss observed for the pre-calcined Fe−Ni/AC catalyst are 11.85% (100 - 300 °C), 65.35% (300−400 °C) and 38.41% (400 - 650 °C), while the percentage weight loss observed on the thermogram curve of the post-calcined catalyst are 6.5% (100 - 300 °C), 50.73% (300−400 °C) and 27.66% (400 - 650 °C). According to the thermogram curve, it is obvious that post-calcined Fe−Ni/AC catalyst may be considered more thermally stable than the pre-calcined Fe−Ni/AC catalyst above the temperature of 600 °C due

to the presence of metallic oxides attached on the surface of the AC support.

The functional groups present in the Fe−Ni/AC catalyst were analyzed by FTIR and the results are shown in Fig. C1b. For the pre-calcined Fe−Ni/AC catalyst, the absorption peaks were observed at 672 cm^{-1}, 1387 cm^{-1}1647 cm^{-1}, 2353 cm^{-1} and 3437 cm^{-1} which corresponds to the strong absorption vibrational stretch at 672 cm^{-1} (C−H), 1387 cm^{-1} (O−H), 1647 cm^{-1} (C=O), 2353 cm^{-1} (C≡C) and 3437 cm^{-1} (O−H). This indicates the presence of alkane, carboxylic, alcohol and phenol (Nadar et al., 2018). The vibrational bands indicates the presence of strong C−H (682 cm^{-1}), O−H (1387 cm^{-1}) C−O (1650 cm^{-1}), C≡C (2354 cm^{-1}) and O−H (3437 cm^{-1}) peaks bending from alkane, carbonyl, carboxylic, alcohol and phenol groups (Nadar et al., 2018). It is significant to note that, three additional peaks were present in the post-calcined Fe−Ni/AC catalyst at 1052 cm^{-1}2074 cm^{-1} and 3122 cm^{-1}. The new peaks are assigned to vibration bonding of O−H (1052 cm^{-1}), C−O (2074 cm^{-1}) and C−H (3122 cm^{-1}) due to aromatics, carbonyl, carboxyl and hydroxyl compound introduced to the Fe−Ni/AC catalyst by calcination process.

The surface morphology and elemental composition of Fe−Ni/AC catalyst was examined using HRSEM coupled with the EDS and the result of the surface morphology of the pre-calcined and post-calcined Fe−Ni/AC catalyst are presented in Fig. C1c and C1d respectively. The HRSEM micrograph of the pre-calcined Fe−Ni/AC catalyst in Fig. C1c revealed the spherically shaped deposition of iron and nickel particles on the surface of activated carbon support with few pores.

However, the surface morphology of the post-calcined Fe−Ni/AC catalyst showed the presence of iron and nickel particles on the surface of AC. The catalyst particles were densely packed and homogenous. Not only that, evidence of pore formation was observed in the post-calcined Fe−Ni/AC compared to the pre-calcined Fe−Ni/AC catalyst. The remarkable pores development and enhancement observed on the surface of post-calcined Fe−Ni/AC catalyst could be attributed to the diffusion of the metallic particles onto the pores of the AC and decomposition of nitrates during calcinations (Acomb et al., 2016).

In addition to the HRSEM analysis on the Fe−Ni/AC catalyst, the result of the elemental composition of the Fe−Ni/AC catalyst is presented in Table E3.

The result of the elemental composition shows that AC support did not decompose during the calcination process. Also, the iron and nickel metallic constituents were enhanced due to the decomposition of nitrates during calcination process. The improved iron and nickel metallic components on the surface of AC support confirm that the Fe−Ni/AC catalyst has the required surface chemistry composition for the synthesis of carbon nanotubes.

3.3. Characterization of MWCNTs and MWCNTs-OCH₂CO₂H

The surface properties of MWCNTs and MWCNTs-OCH₂CO₂H was investigated and the result revealed that the BET surface area, total pore volume and average pore diameter of MWCNTs were 1250 m^2/g, 0.84 cm^3/g and 30 nm, respectively. However, the BET surface area, total pore volume and average pore diameter of MWCNTs-OCH₂CO₂H were obtained as 1172 m^2/g, 0.61 cm^3/g and 25 nm, respectively. The dense coverage of the surface of MWCNTs-OCH₂CO₂H by −OCH₂CO₂H groups after carboxylation which occupied the tubular structural network could be responsible for the observed reduction in the surface area, pore size and pore volume. Similar observation was made by Yang et al. (2018) that reported decrease in surface parameters of MWCNTs@SiO₂−NH₂ after amination reaction. The BET result shows consistency with the FTIR, TGA, XPS, HRSEM and HRTEM result that confirmed successful

grafting of carboxylic groups on the MWCNTs-OCH₂CO₂H.

The FTIR spectra of MWCNTs and MWCNTs-OCH₂CO₂H was investigated and presented in Fig. 1a.

The strong band at the wave numbers of 1603 cm^{-1} and 1765 cm^{-1} on the MWCNTs-OCH₂CO₂H were ascribed to the stretching and bending vibration of C=O due to the presence of carboxylic acid. Other additional absorption bands on the MWCNTs-OCH₂CO₂H were associated with the stretching adsorption at 1158 (C−O), 1255 (C−O), 2000 (C≡C) and 2190 (C≡C) and are related to the −COOH groups. Incidentally, the adsorption peak at 2071 cm^{-1} (C≡C) on the MWCNTs disappeared after carboxylation and the disappearance may be linked to the carboxylation phenomenon (Fig. 1a). In addition, it was observed that the adsorption peaks at 2456, 2721, 2990, 3740 and 3860 cm^{-1} which correspond to C≡C, C−H and −OH stretching vibration were consistent on both the MWCNTs and MWCNTs-OCH₂CO₂H (Huang et al., 2019). However, the vibration bands on the MWCNTs-OCH₂CO₂H were more pronounced, which may be attributed to the functional groups incorporated on the surface of MWCNTs through carboxylation (Jiang et al., 2016). Similar trends in FTIR analysis have been reported in other MWCNTs and functionalization studies (Zheng et al., 2018), thereby confirming the successful synthesis of MWCNTs and grafting of CH₂BrCO₂H groups onto the MWCNTs.

The TGA curves corresponding to the loss in the mass of MWCNTs and MWCNTs-OCH₂CO₂H as a function of temperature is shown in Fig. 1b. Two distinct stages of decomposition were observed on the nano-adsorbents. In MWCNTs, the initial weight loss of 5.5 wt% was observed between the temperatures of 50 °C to 345 °C and was attributed to the evaporation of water. As the temperature increased further from 345 °C to 540 °C, a significant weight loss of 64.2 wt% was observed by the MWCNTs due to the decarboxylation, volatilization and graphitization of the functional groups (Jun et al., 2018). On the other hand, Fig. 1b revealed that MWCNTs-OCH₂CO₂H decomposed faster than MWCNTs due to the formation of oxygenated functional groups on the surface of MWCNTs-OCH₂CO₂H during carboxylation. At the temperature range of 50 °C to 300 °C, a negligible weight loss of 1.2 wt% was ascribed to the evaporation of adsorbed moisture. In addition, rapid weight loss of 65.5 wt% occurred when temperature was increased from 300 °C to 450 °C, and such loss was attributed to oxidation of amorphous carbon and transformation of metallic impurities from the catalyst support. Beyond the temperatures of 540 °C and 450 °C, the weight loss of the MWCNTs and MWCNTs-OCH₂CO₂H were observed to exhibit insignificant profile reduction due to the loss of the residual inorganic and organic compounds. The obtained result showed that the functional groups were successfully incorporated on the surface of MWCNTs and further corroborates the FTIR and XPS results. Also, this findings agreed with previously reported thermal decomposition profiles of MWCNTs and functionalized MWCNTs (Jun et al., 2018).

Crystalline nature and phase purity of MWCNTs and MWCNTs-OCH₂CO₂H were investigated by XRD and corresponding XRD pattern is shown in Fig. 1c. According to the XRD results, MWCNTs was found to be crystalline in nature due to the formation of sharp diffraction peaks at 2 theta values 26.22°, 43.63° and 50.50°, which correspond to the following crystal planes (002), (101) and (102). These peaks matched well with a typical graphitic carbon (Jiang et al., 2016). Also, the crystal planes of the peaks were aligned to the following interlayer spacing 3.4 nm (002), 2.07 nm (101) and 1.8 nm (102). After carboxylation reaction, MWCNTs-OCH₂CO₂H material possessed three sharp diffraction peaks (26.22°, 43.63° and 50.50°) and two weak peaks (32.18° and 46.25°) assigned to the following crystal planes (002), (101), (102), (111) and (222) (Fig. 1c). The formation of these peaks (32.18° and 46.25°) with the following interlayer spacing 2.78 nm and 1.96 nm could be attributed to
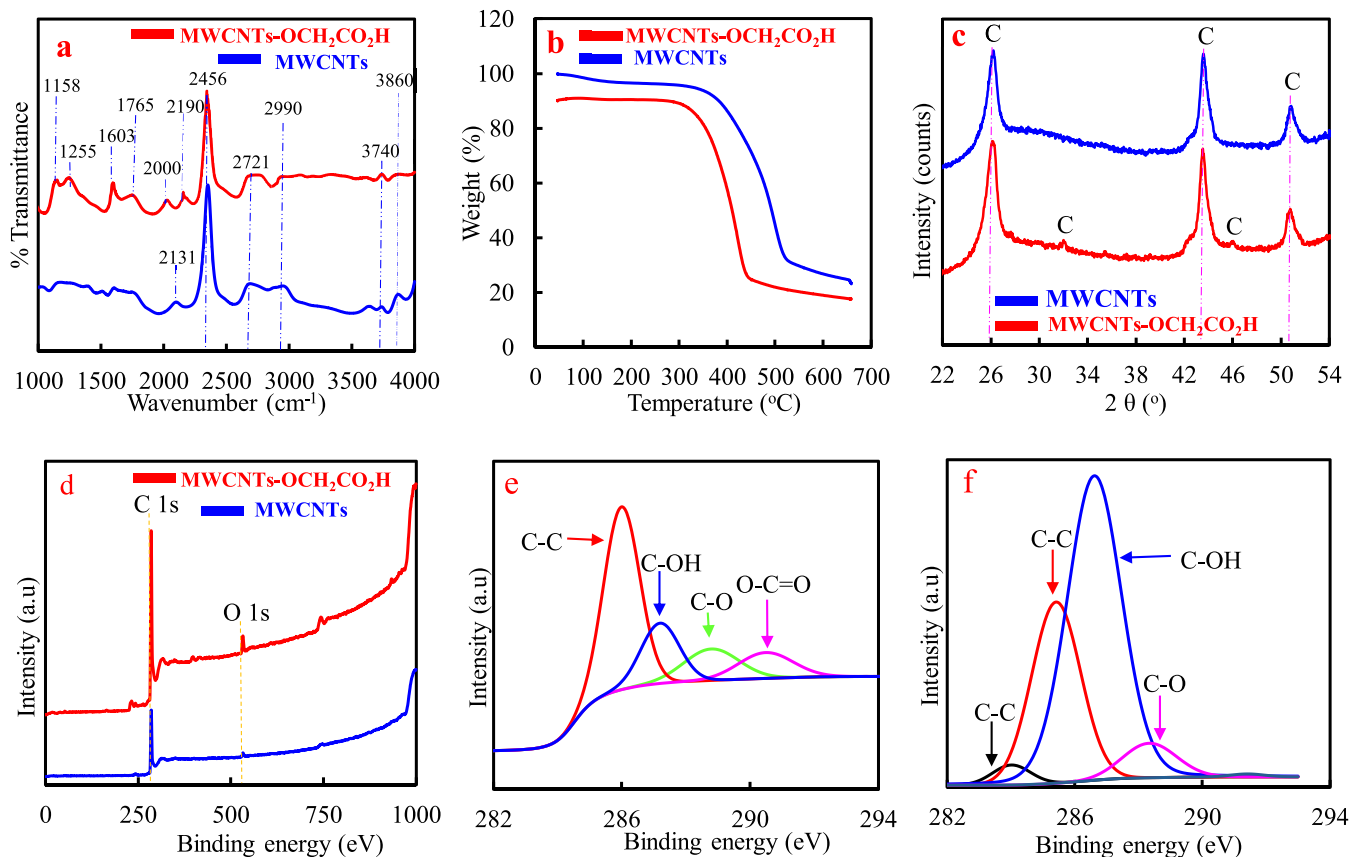
Fig. 1. (a) FTIR; (b) TGA; (c) XRD; (d) XPS spectra of MWCNTs and MWCNTs-OCH₂CO₂H; (e) high-resolution C 1s XPS spectra of MWCNTs and (f) high-resolution C 1s XPS spectra of MWCNTs-OCH₂CO₂H.

carboxylation reaction. The peaks corroborated the previously reported crystalline and clear structure of MWCNTs and MWCNTs-OCH₂CO₂H respectively (Kang et al., 2018; Wu et al., 2020). This implies that the carboxylation procedure did not destroy the crystalline and the crystals lattice structure of the MWCNTs. The crystallite sizes of MWCNTs according to Debye-Scherrer equation were determined to 4.21, 6.81 and 9.65 nm, with an average of 6.89 nm. For the MWCNTs-OCH₂CO₂H, 5.62, 8.57, 10.11, 13.25 and 21.83 nm was estimated as the crystallite sizes. An average crystallite size of 11.88 nm was obtained for the MWCNTs-OCH₂CO₂H. The increase in the crystallite size of MWCNTs-OCH₂CO₂H could be linked to the incorporated CH₂BrCOOH through carboxylation of MWCNTs.

XPS analysis identifies the functional groups and the elements present on the surface of nano-adsorbents. Further confirmation of successful grafting of CH₂BrCOOH onto the MWCNTs are displayed in the XPS spectra. Fig. 1d shows the presence of C (1s) and O (1s) spectra, thereby indicating that carbon and oxygen were the dominant elements on the surface of MWCNTs and MWCNTs-OCH₂CO₂H. The C (1s) and O (1s) peaks appeared at the binding energies of 284.5 eV and 533 eV, respectively. However, it was noticed that there was an increased in the intensity of the C (1s) and O (1s) peaks in the XPS spectra of MWCNTs-OCH₂CO₂H and may be attributed to the improved functional groups due to carboxylation (Zhao et al., 2019a, 2019b). The deconvoluted peaks of the high resolution C (1s) spectrum for the MWCNTs and MWCNTs-OCH₂CO₂H are presented in Fig. 1e and f. According to Fig. 1e, the C (1s) spectrum of MWCNTs revealed the presence of the following functional groups (C−C), (C−OH), (C−O) and (O−C═O) at the

binding energies of 286.1, 287.3, 288.9 and 290.6 eV.

In the same vein, Fig. 1f which depict the XPS spectrum of MWCNTs-OCH₂CO₂H revealed the presence of the following functional groups at 284.0 (C−C), 285.6 (C−C), 286.8 (C−OH) and 288.4 (C−O). Comparatively, the differences in the binding energies of similar functional groups on MWCNTs and MWCNTs-OCH₂CO₂H suggested shift in absorption peaks due to carboxylation of the latter than the former. Also, it was observed that carboxylation enhanced oxygen loss of O−C═O, which resulted to overall decrease in oxygen content. The functional group revealed by the XPS result corresponds with the FTIR result in Fig. 1a.

The HRSEM and HRTEM images of MWCNTs and MWCNTs-OCH₂CO₂H are shown in Fig. 2(a−h).

According to Fig. 2a, b, e and f, it can be found that some MWCNTs contacted closely with each other forming network of aggregates. The result showed a curved, tubular and tangled structural network. Remarkably, distinguishable morphological structures were identified on the surface of MWCNTs-OCH₂CO₂H through the HRSEM and HRTEM, which could be linked to the effect of carboxylation. Compared to Fig. 2 (a and e), Fig. 2 (b and f) clearly revealed a decrease in the degree of the structural aggregation which could be due to carboxylation. In addition, the diameter of carbon nanotubes obtained through HRTEM (Fig. 2e and f) increased from 15 to 30 nm and 45−50 nm after carboxylation. The result suggests that the surface of MWCNTs-OCH₂CO₂H was heavily covered by carboxylic groups. After adsorption, the HRSEM (Fig. 2c and d) and HRTEM (Fig. 2g and h) images revealed the closely packed tubular morphology and deposition of the adsorbed As(V) and Mn(VII) ions. Correspondingly, the electrostatic repulsion
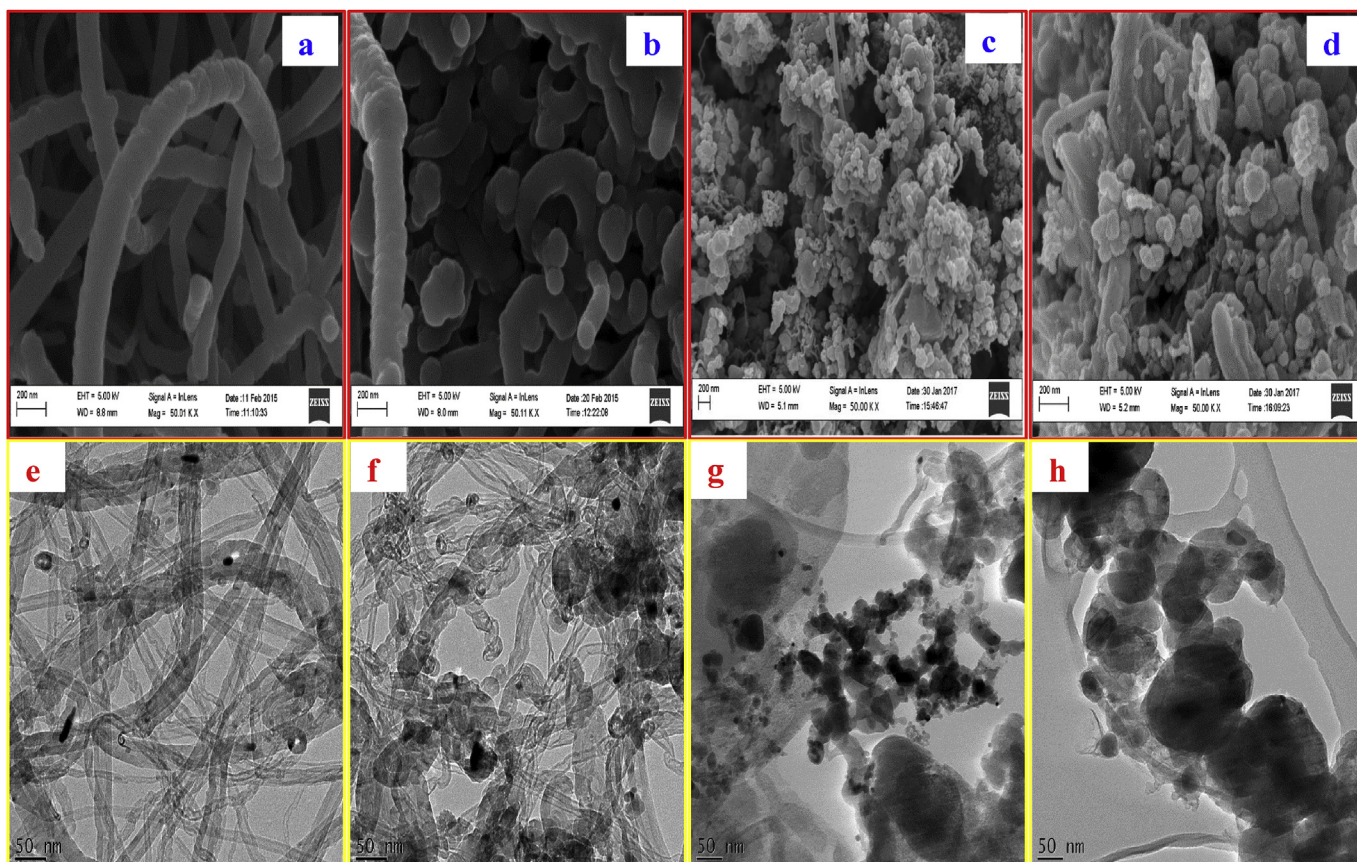
Fig. 2. HRSEM (a, b, c, d) and HRTEM (e, f, g, h) images of (a, e) MWCNTs; (b, f) MWCNTs-OCH₂CO₂H; (c, g) MWCNTs after adsorption of As(V) and Mn(VII)and (d, h) MWCNTs-OCH₂CO₂H after adsorption of As(V) and Mn(VII).

existing between −OCH$_2$CO$_2$H groups and the oxygen via carboxylation possibly increased the closed tubular packing. After the adsorption of As(V) and Mn(VII), the electrostatic repulsion weakened despite the increased tubular packing due to multiple interactions with the adsorption sites (Zhao et al., 2019a, 2019b). The observed changes in morphology suggests that carboxylation procedure enhanced the close tubular packing, therefore, the carboxyl group strengthen the MWCNTs-As(V) and MWCNTs-Mn(VII) interaction.

3.4. Investigation of parametric effects on the As(V) and Mn(VII) adsorption

3.4.1. Effect of contact time on As(V) and Mn(VII) adsorption

The influence of contact time on adsorption capacity of MWCNTs and MWCNTs-OCH$_2$CO$_2$H for the removal of As(V) and Mn(VII) in chemical industrial wastewater was investigated and the result is presented in Fig. 3a. As revealed in Fig. 3a, the adsorption capacities of MWCNTs and MWCNTs-OCH$_2$CO$_2$H for As(V) and Mn(VII) increased rapidly within first 60 min. This rapid increase in adsorption at this time domain could be attributed to the external diffusion of As(V) and Mn(VII) to the massive number of adsorption sites and the existence of strong electrostatic attraction between the heavy metals and the nano-adsorbents. Beyond 60 min, there was insignificant increase in the adsorption capacity due to the influence of intraparticle diffusion and the saturation of the active sites on the nano-adsorbents surface (Kazak et al., 2018). In this study, equilibrium adsorption capacity was achieved in 60 min for both As(V) and Mn(VII) adsorption onto MWCNTs and MWCNTs-

OCH$_2$CO$_2$H. Moreover, negligible adsorption of As(V) and Mn(VII) onto the nano-adsorbents were observed after 60 min. As shown in Fig. 3a, the adsorbed quantity of As(V) and Mn(VII) onto MWCNTs increased from 176 to 215 mg/g and 139−211 mg/g. In the same vein, the uptake of As(V) and Mn(VII) equally increased from 196 to 271 mg/g and 184−260 mg/g for MWCNTs-OCH$_2$CO$_2$H. Generally, the removal efficiency of As(V) and Mn(VII) from the wastewater using MWCNTs-OCH$_2$CO$_2$H, was higher compared to MWCNTs. This could be attributed to the increase in functional groups on the surface of the former than the latter. The trend of this result showed that the adsorption behavior of the MWCNTs and MWCNTs-OCH$_2$CO$_2$H were not dependent on the surface area, but also on the functionalities of each nano-adsorbent.

Accordingly, MWCNTs-OCH$_2$CO$_2$H with surface area of 1172 m^2/g adsorbed more As(V) and Mn(VII) compared with MWCNTs with higher surface area of 1250 m^2/g. Similar observation was made by Xu et al. (2018) in the adsorption of heavy metals using functionalized carbon nanotubes and graphene.

3.4.2. Effect of dosage on As(V) and Mn(VII) adsorption

The influence of nano-adsorbent dosage on the uptake of As(V) and Mn(VII) ions by MWCNTs and MWCNTs-OCH$_2$CO$_2$H was studied and the result presented in Fig. 3b. The result demonstrated a rapid uptake of As(V) and Mn(VII) ions from wastewater when the nano-adsorbent dose was increased from 10 to 30 mg for both MWCNTs and MWCNTs-OCH$_2$CO$_2$H. The increment may be due to increase in the number of adsorption sites and the surface functional groups (Jun et al., 2019). However, further increase in nano-adsorbent dosage from 40 to 60 mg did not result to any significant
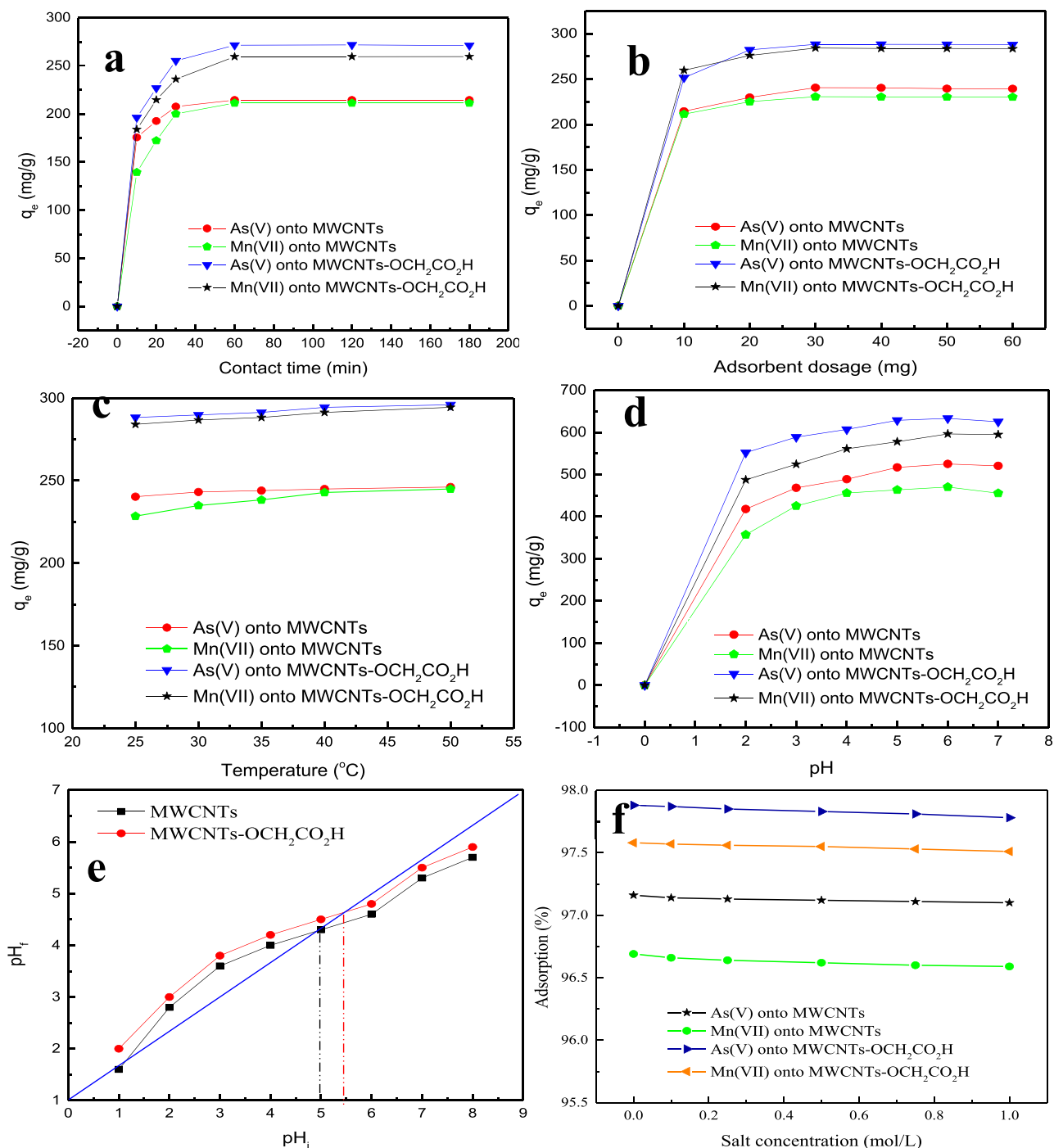
Fig. 3. Influence of (a) contact time, (b) adsorbent dosage, (c) temperature, (d) pH on As(V) and Mn(VII) adsorption onto MWCNTs and MWCNTs-OCH$_2$CO$_2$H, (e) Point of zero charge (pH$_{PZC}$) determined by pH drift method and (f) impact of ionic strength (KNa) on As(V) and Mn(VII) adsorption efficiency by MWCNTs and MWCNTs-OCH$_2$CO$_2$H at adsorbent dosage (30 mg), contact time (60 min) and temperature (50 °C).

increase in the adsorption of As(V) and Mn(VII) and this may was linked to the aggregation that limited the active sites of the nano-adsorbents (Kazak et al., 2018). Notably, maximum removal of As(V) and Mn(VII) by the nano-adsorbents were achieved using 30 mg dose. More specifically, Fig. 3b revealed that the adsorption capacities of As(V) and Mn(VII) increased from 215 to 240 mg/g and 211−231 mg/g for MWCNTs. Similar trend of increment in adsorption capacity from 251 to 288 mg/g and 259−284 mg/g for MWCNTs-OCH$_2$CO$_2$H. In comparison, MWCNTs-OCH$_2$CO$_2$H had

better adsorption capacity for As(V) and Mn(VII) than MWCNTs. Although MWCNTs had a large surface area (1250 m^2/g) compared to MWCNTs-OCH$_2$CO$_2$H (1172 m^2/g). This suggest that adsorption phenomenon in this study largely depend on the functional groups and not the surface area of the nano-adsorbents. The result of the adsorption capacity further indicates that strong electrostatic attraction was the main mechanism of As (V) and Mn(VII) adsorption, and not weak physical surface area. Also, it was also found that at every dosage of the nano-adsorbents under the
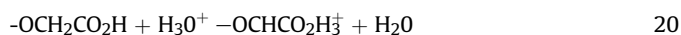
applied conditions, more of As(V) was removed than Mn(VII), due to the smaller ionic radius of (0.46 Å) than Mn(VII) with higher ionic radius of (0.66 Å). Studies have shown that metal with smaller ionic radius diffused faster through the pores of the adsorbent than metal with high ionic radius (Lima et al., 2019).

3.4.3. Effect of temperature on As(V) and Mn(VII) adsorption

Temperature influence on the adsorption of As(V) and Mn(VII) by MWCNTs and MWCNTs-OCH$_2$CO$_2$H was examined and the result shown in Fig. 3c. According to the result, increase in temperature had a significant effect on the removal of As(V) and Mn(VII) using the nano-adsorbents and 50 °C was found to be the optimum adsorption temperature. Above all, adsorption capacity of As(V) and Mn(VII) increased from 240 to 246 mg/g and 229–245 mg/g for MWCNTs, similarly an increase from 288 to 296 mg/g and 284–296 mg/g was observed for MWCNTs-OCH$_2$CO$_2$H. It was noticed that the adsorption of the two heavy metal ions using MWCNTs and MWCNTs-OCH$_2$CO$_2$H were favorable due to the endothermic nature of the reaction. This may be due to the decrease in solution viscosity, which favored external mass transfer and diffusion of the As(V) and Mn(VII) onto the pores of the nano-adsorbents. Furthermore, increase in temperature of the medium resulted to increase in kinetic energy and rapid collision of As(V) and Mn(VII) with the active surface sites of the nano-adsorbent. This by extension improved the interaction of As(V) and Mn(VII) with the surface functional groups of MWCNTs and MWCNTs-OCH$_2$CO$_2$H respectively. Comparatively, As(V) and Mn(VII) adsorption was higher using MWCNTs-OCH$_2$CO$_2$H, compared to MWCNTs and this could be linked to the large adsorption sites from the incorporated functional groups on the MWCNTs-OCH$_2$CO$_2$H.

3.4.4. Effect of pH on As(V) and Mn(VII) adsorption

pH is an important adsorption parameter that affects the solubility of heavy metal ions in aqueous solutions and the activity of the functional groups (Yang et al., 2018). The effect of pH on the As(V) and Mn(VII) adsorption using MWCNTs and MWCNTs-OCH$_2$CO$_2$H was evaluated and the result illustrated in Fig. 3d. With the pH increase from 2 to 6, the As(V) and Mn(VII) adsorption capacity of MWCNTs increased from 418 to 525 mg/g and 357–470 mg/g, respectively. Similarly, the adsorption capacity of As(V) and Mn(VII) increased from 552 to 633 mg/g and 487–596 mg/g using MWCNTs-OCH$_2$CO$_2$H as the pH was adjusted from 2 to 6. It was also observed that beyond the pH of 6, the adsorption of the two heavy metal ions by the nano-adsorbents was highly negligible. The low adsorption capacity at low pH (>6) may be attributed to the strong electrostatic repulsion between the hydronium ions and As(V) and Mn(VII) in strong acidic conditions which led to the protonation of oxygen containing groups (Jiang et al., 2016). Basically, the competition at low pH prevented the metal ions from adsorbing on the adsorption sites of the nano-adsorbent. This process is represented in Eq. (20).

$$\text{-OCH}_2\text{CO}_2\text{H} + \text{H}_3\text{O}^+ \ \text{-OCHCO}_2\text{H}_3^{\ddagger} + \text{H}_2\text{O} \qquad 20$$

Furthermore, the high adsorption of As(V) and Mn(VII) at the basic pH range may be due to low concentration of H+ ion and less competition with metal ions for adsorption onto negatively charged surfaces of the nano-adsorbents. The adsorptive behavior of the two nano-adsorbent with respect to solution pH can be related to the point of zero charge (pH$_{PZC}$) which determines charge on the surface of nano-adsorbent at a particular pH. It also aids the understanding of the possible electrostatic interactions between the adsorbate species and the adsorbent in water. The pH$_{PZC}$ for the MWCNTs and MWCNTs-OCH$_2$CO$_2$H was evaluated and the result presented in Fig. 3e. As demonstrated in Fig. 3e, the pH$_{PZC}$ for the

MWCNTs and MWCNTs OCH$_2$CO$_2$H were obtained as 5 and 5.5 respectively. This indicates that the surface of the nano-adsorbents was positively charged at pH < 5 and 5.5, depicting strong electrostatic repulsion between the heavy metal ions (As(V) and Mn(VII)) and the positively charged surface of the nano-adsorbents. On the other hand, the MWCNTs and MWCNTs-OCH$_2$CO$_2$H surface became negatively charged at pH > 5 and 5.5, thereby enhancing the rate of As(V) and Mn(VII) adsorption onto the nano-adsorbents due to weak electrostatic force of repulsion (Yang et al., 2018). The results of this study shows that As(V) and Mn(VII) adsorption from industrial chemical wastewater using MWCNTs and MWCNTs-OCH$_2$CO$_2$H is highly pH dependent. Similar observation was also made by Liu et al. (2018) in the investigation of As(V) adsorption using ZrO(OH)$_2$/CNTs.

3.4.5. Effect of ionic strength on As(V) and Mn(VII) adsorption

It is important to investigate the effect of ionic strength and various electrolytes on the equilibrium adsorption capacity because of the followings: firstly, the composition of the solutions affects surface charge on the MWCNTs and MWCNTs-OCH$_2$CO$_2$H; secondly, the possibility of competition between the positive ions (K and Na) and the metal ions (As (V) and Mn (VII)); and thirdly, high ionic strength may result to the aggregation of the nano-adsorbents (Jun et al., 2019). The impact of Ionic strength on the adsorption of As(V) and Mn(VII) by MWCNTs and MWCNTs-OCH$_2$CO$_2$H was evaluated and the result presented in Fig. 3f. As shown in Fig. 3f, the influence of ionic strength on the As(V) and Mn(VII) adsorption on the nano-adsorbents was very negligible. This implies that As (V) and Mn(VII) was attracted more to the surface of MWCNTs and MWCNTs-OCH$_2$CO$_2$H, than K$^+$ and Na$^+$. This may be attributed to the monovalent nature of the electrolyte, compared to pentavalent and heptavalent nature of the adsorates: As(V) and Mn(VII) that would presumably have higher electrostatic attraction (Zhao et al., 2019a, 2019b). Also, the ionic radius of As(V) and Mn(VII) are 0.46 and 0.66 Å, while the ionic radius of K$^+$ and Na$^+$ are 1.55 and 0.95 Å. Therefore, As(V) and Mn(VII) with smaller ionic radius adsorbed more on the surface of MWCNTs and MWCNTs-OCH$_2$CO$_2$H because the electrostatic interactions occurring between penta and heptavalence elements were much larger than those between the adsorbent and mono valence electrolytes (K$^+$ and Na$^+$) (Jun et al., 2019). In addition, the electronegativity value of As^{+5} (2.18) and Mn^{+7} (1.55) were higher than that of K (0.82) and Na (0.93), indicating that As(V) and Mn(VII) removal was faster than K$^+$ and Na$^+$.

3.5. Adsorption isotherm

To further investigate the adsorption performance of the interaction of As(V) and Mn(VII) with the MWCNTs and MWCNTs-OCH$_2$CO$_2$H, isotherm models such as Langmuir, Freundlich, Temkin and D-R were employed to correlate the experimental data obtained at equilibrium. The analysis of the raw industrial wastewater revealed that the initial concentration of As(V) and Mn(VII) were 92.00 and 76.00 mg/L. After treatment, the concentration obtained at equilibrium (C$_e$) for As(V) and Mn(VII) was 0.13 and 0.24 mg/L for MWCNTs. Also, the C$_e$ for As(V) and Mn(VII) using MWCNTs-OCH$_2$CO$_2$H was 0.02 and 0.10 mg/L respectively. The obtained concentrations of As(V) and Mn(VII) on both nano-adsorbents were lower than their permissible standard concentration of 0.20 and 0.50 mg/L in water by EPA and WHO (US EPA, 2012; WHO, 2017). The fitting results of the adsorption isotherms of As(V) and Mn(VII) onto MWCNTs and MWCNTs-OCH$_2$CO$_2$H are shown in Figs. C2(a-d), C3, C4, C5 and Table 2.

As revealed by the results, Langmuir model better described the adsorption isotherms of As(V) and Mn(VII) on MWCNTs and MWCNTs-OCH$_2$CO$_2$H than the other models based on the values of

Table 3
Comparison of maximum adsorption capacity and BET surface area for MWCNTs and MWCNTs-OCH$_2$CO$_2$H with various adsorbents described in the literature.

Adsorbent	Heavy metal	q$_m$ (mg/g)	S$_{BET}$ m^2/g	Isotherm	Kinetics	Particle size (nm)	Reference
MnFe$_2$O$_4$NPs	As(V)	27.65	81.09	Freundlich	pseudo-second order	50	Martinez−Vargas et al. (2018)
Fe-MWCNTs	As(V)	250	–	Freundlich	pseudo-first order	–	Alijani and Shariatinia (2017)
GACPMF	As(V)	9.52	736.20	Langmuir	pseudo-second order	–	Roh et al. (2018)
ZrO(OH)$_2$/CNTs	As(V)	124.60	126.00	Langmuir	pseudo-second order	1−8	Liu et al. (2018)
GO/CuFe$_2$O$_4$	As(V)	124.69	–	Langmuir	–	–	Wu et al. (2018)
FeOx-GO	As(V)	113.00	341.00	Langmuir	pseudo-second order	5	Su et al. (2017)
FCNT-HOX	As(V)	6.37	169.00	Langmuir	pseudo-second order	–	Sankararamakrishnan et al. (2014)
Af-NPC/MnO$_2$	As(V)	9.43	633.00	Langmuir	pseudo-second order	–	Pathan et al. (2016)
Fe-Purnice	Mn(VII)	7.14	–	Langmuir	–	–	Çifçi and Meriç (2017)
NZ	Mn(VII)	31.20	112	Langmuir	–	–	Ates and Akgül (2015)
Marine nanosediment	Mn(VII)	49.20	6.26	Langmuir	Pseudo-second order	40−60	Mahmoud et al. (2019)
MWCNTs	As(V)	200	1250	Langmuir	pseudo-second order	30	This study
MWCNTs	Mn(VII)	192	1250	Langmuir	pseudo-second order	30	This study
MWCNTs OCH$_2$CO$_2$H	As(V)	250	1172	Langmuir	pseudo-second order	50	This study
MWCNTs OCH$_2$CO$_2$H	Mn(VII)	236	1172	Langmuir	pseudo-second order	50	This study

coefficient of correlation (R^2) and error analysis (X^2 and SSE). Overall, Langmuir isotherm affirmed a homogenous and monolayer coverage by both MWCNTs and MWCNTs-OCH$_2$CO$_2$H, indicating the chemisorptions behavior of the adsorption of As(V) and Mn(VII) respectively. The maximum adsorption capacity (q$_m$) of As(V) and Mn(VII) adsorption onto MWCNTs obtained from Langmuir isotherm was 200 and 192 mg/g, while As(V) and Mn(VII) adsorption onto MWCNTs-OCH$_2$CO$_2$H was 250 and 238 mg/g respectively. From the results of the calculated isotherm parameters in Table 2, carboxylation greatly improved the adsorption capacity of As(V) onto MWCNTs (200 mg/g) to 250 mg/g for MWCNTs-OCH$_2$CO$_2$H.

Similarly, the adsorption of Mn(VII) also increased from 192 mg/g for MWCNTs to 238 mg/g for MWCNTs-OCH$_2$CO$_2$H. This shows that the presence of more functional groups on the carboxylated MWCNTs improved the binding sites and the adsorption efficiency of Mn(VII) on the nano-adsorbent. The observed large adsorption capacity of As(V) over Mn(VII) on both nano-adsorbent could be due to varying adsorption mechanisms, for instance Mn(VII) basically formed bidentate complexes, while As(V) mostly forms monodenate complexes on the adsorbent surface with the hydroxyl groups (Liu et al., 2018). Compared to the literature results shown in Table 3, MWCNTs and MWCNTs-OCH$_2$CO$_2$H was found to be more efficient adsorbents for the sorption of As(V) and Mn(VII) from industrial wastewater. With the exception of the work of Alijani and Shariatinia (2017) that reported maximum adsorption capacity of 250 mg/g in the adsorption of As(V) from stock solution of arsenic as a simulated wastewater using Fe-MWCNTs, the result of this study was higher than the adsorption capacity reported by previous researchers as shown in Table 3. Meanwhile, real wastewater was used in this study which contains scavengers such as carbonates, sulphates, phosphates, chlorides, nitrates that also compete for the adsorptive sites with the metal ions of interest. This is however not the case with simulated wastewater which contain none of these scavengers and as such the adsorptive performance in the simulated wastewater will be higher than real industrial wastewater. Similarly, Martinez−Vargas et al. (2018) and Alijani and Shariatinia (2017) also reported fitness of their experimental data to Freundlich isotherm, where as other studies collaborated with the Langmuir isotherm model reported in this research.

Table 4
Kinetic models calculated parameters for As(V) and Mn(VII) adsorption onto MWCNTs and MWCNTs-OCH$_2$CO$_2$H.

Kinetics	Parameters	MWCNTs		MWCNTs-OCH$_2$CO$_2$H	
		As(V)	Mn(VII)	As(V)	Mn(VII)
PFO	q$_{e,exp}$ (mg/g)	214.449 ± 1.015	211.364 ± 2.020	259.683 ± 2.500	251.773 ± 2.010
	q$_{e,cal}$ (mg/g)	32.9762 ± 1.300	1915.140 ± 1.200	105.974 ± 1.100	17.386 ± 1.200
	K$_1$ (g mg^{-1} min^{-1})	−0.037 ± 0.002	−0.215 ± 0.001	−0.078 ± 0.004	−0.023 ± 0.003
	R^2	0.675	0.948	0.992	0.535
	SSE	33.132	311.065	28.063	42.793
	X^2	998.675	1515.740	222.944	3159.860
PSO	q$_{e,cal}$ (mg/g)	222.222 ± 1.002	217.391 ± 1.004	263.157 ± 1.003	256.410 ± 1.001
	K$_2$ (g mg^{-1} min^{-1})	0.001 ± 0.0001	0.001 ± 0.0002	0.002 ± 0.0001	0.002 ± 0.0002
	h$_0$ (mg g^{-1} min^{-1})	58.14 ± 1.001	55.870 ± 3.002	144.930 ± 2.001	135.14 ± 1.000
	R^2	1.000	0.999	1.000	1.000
	SSE	1.419	1.101	0.634	0.847
	X^2	0.272	0.167	0.046	0.084
Elovich	q$_{e,cal}$ (mg/g)	1801.146 ± 2.400	793.691 ± 1.500	214346.840 ± 2.200	44,184.980 ± 2.300
	α (g mg^{-1} min^{-2})	1801.146 ± 2.400	793.691 ± 1.500	214346.841 ± 2.200	44,184.981 ± 2.300
	β (mg g^{-1} min^{-1})	0.037 ± 0.006	0.033 ± 0.004	0.050 ± 0.005	0.045 ± 0.003
	R^2	0.938	0.905	0.914	0.865
	SSE	289.689	106.318	39,086.788	8021.070
	X^2	1397.780	427.251	213,827.789	43,682,086.,8278,68268
IPD	q$_{e,cal}$ (mg/g)	153.900 ± 1.300	147.280 ± 1.400	217.080 ± 1.200	205.820 ± 1.100
	k$_t$ (g mg^{-1} min^{-1})	5.796 ± 0.004	5.796 ± 0.003	3.842 ± 0.002	3.842 ± 0.001
	C (mg/g)	147.280 ± 0.300	147.280 ± 0.400	217.080 ± 0.600	217.080 ± 0.500
	R^2	0.611	0.611	0.626	0.626
	SSE	11.055	11.700	7.778	8.390
	X^2	23.822	27.884	8.361	10.260

3.6. Adsorption kinetics

The experimental data obtained for the adsorption of As(V) and Mn(VII) onto MWCNTs and MWCNTs-OCH$_2$CO$_2$H were fitted to the non-linear pseudo-first order, pseudo-second order, Elovich and intraparticle diffusion kinetic models as presented in Fig. C2(e and f) and C6. Also, the parameters of the kinetic models were evaluated for the best fit based on the values obtained for the R^2, SSE and X^2 as shown in Table 4.

Particularly in Table 4, pseudo-second-order kinetic model showed best correlation with experimental data compared to other kinetic models as revealed by the high R^2, low error (SSE and X^2) values and substantial relationship between the experimental and calculated adsorption capacity. The adsorption of As(V) and Mn(VII) from industrial wastewater onto the MWCNTs and MWCNTs-OCH$_2$CO$_2$H at the initial contact time were better described by pseudo-second order model due to its high values of the initial rates of adsorption (h0). Equally, the calculated k_2 values confirmed fast adsorption of As(V) and Mn(VII) onto the MWCNTs and MWCNTs-OCH$_2$CO$_2$H. Meanwhile, the higher values of α compared to the lower values of β in Elovich model suggests higher adsorption than desorption process and higher affinity of As(V) and Mn(VII) to MWCNTs and MWCNTs-OCH$_2$CO$_2$H.

In intraparticle diffusion, the high values of C were attributable to the rapid adsorption of As(V) and Mn(VII) onto the exterior surface of MWCNTs and MWCNTs-OCH$_2$CO$_2$H. The evaluated kinetic parameters in this study suggest that the adsorption process of As(V) and Mn(VII) by MWCNTs and MWCNTs-OCH$_2$CO$_2$Hwas strongly driven by chemical interaction (Lima et al., 2019). Therein, As(V) and Mn(VII) adsorption onto MWCNTs-OCH$_2$CO$_2$H showed better adsorption parameters compared to MWCNTs due to the effect of carboxylation process. According to the comparative study of the literature results in Table 3, pseudo-second order kinetic model obtained in this study agreed with the work of most researchers, except Alijani and Shariatinia (2017) that reported pseudo-first order kinetics in the adsorption of As(V) onto Fe-MWCNTs.

3.7. Thermodynamics investigation

To analyze the thermodynamic parameters of As(V) and Mn(VII) by MWCNTs and MWCNTs-OCH$_2$CO$_2$H, the thermodynamic plots are presented in Fig. C2(g and h), while the values of the calculated parameters are shown in Table 5. As observed from Table 5, ΔG° showed negative values at the various temperature ranges, which also increased with rise in temperature.

The negative values of ΔG° depict the spontaneous nature of As(V) and Mn(VII) adsorption onto MWCNTs and MWCNTs-OCH$_2$CO$_2$H, while the decrease in ΔG° with rise in temperature suggested better adsorption at elevated temperatures. Also, the positive value for ΔH° indicated the endothermic nature of As(V) and Mn(VII) adsorption by MWCNTs and MWCNTs-OCH$_2$CO$_2$H. In addition, positive values of ΔH° implies increase in spontaneity due to As(V)/Mn(VII) interaction with MWCNTs and MWCNTs-OCH$_2$CO$_2$H during the adsorption. It was reported that the values of ΔH° are in the range of 1–40 kJ/mol for adsorption controlled by physisorption, while the values higher than 40 kJ/mol indicate chemisorption (Cheng et al., 2017). Therefore, the adsorption of As(V) and Mn(VII) by MWCNTs and MWCNTs-OCH$_2$CO$_2$H were chemisorption controlled because the obtained values of ΔH° for As(V) and Mn(VII) adsorption by MWCNTs are 263.46 and 494.09 kJ/mol. Similarly, 194.45 and 196.72 kJ/mol were obtained as the ΔH° for As(V) and Mn(VII) adsorption onto MWCNTs-OCH$_2$CO$_2$H. Furthermore, positive values of ΔS° demonstrated increase in randomness at the interface of As(V)/Mn(VII)-MWCNTs/MWCNTs-OCH$_2$CO$_2$H solution.

3.8. Reusability

The reusability of MWCNTs and MWCNTs-OCH$_2$CO$_2$H in adsorbing As(V) and Mn(VII) from industrial wastewater was evaluated through regeneration studies. Reusability is a major economic factor that determines the stability of adsorbents in maintaining high adsorption capacity after several cycles of adsorption (Jun et al., 2019). Therefore, Fig. 4a and b shows the adsorption efficiency of MWCNTs and MWCNTs-OCH$_2$CO$_2$H over 6 cycles.

After the first regeneration cycle, the adsorption capacity of As(V) and Mn(VII) by MWCNTs slightly decreased to 87 and 84%, while As(V) and Mn(VII) adsorption by MWCNTs-OCH$_2$CO$_2$H decreased to 91 and 95% respectively. These values were almost constant up to 5 cycles. However, after the sixth adsorption cycle, As(V) and Mn(VII) adsorption efficiency reduced further to 84 and 80% by MWCNTs and 93 and 90% by MWCNTs-OCH$_2$CO$_2$H respectively. The decrease in adsorption capacity during the repeated applications could be ascribed to wrapping and stacking of MWCNTs tubes, which blocked the accessibility of As(V) and Mn(VII) to the adsorption sites (Zhao et al., 2019a, 2019b). The wrapped and stacked tubular structure of the regenerated MWCNTs and MWCNTs-OCH$_2$CO$_2$H are shown in Fig. 4c and d. In addition, the reduction in adsorption efficiency during the regeneration cycles could be traced to the dominance of the adsorption sites by As(V) and Mn(VII), thus hindering further adsorption of new As(V) and Mn(VII). Furthermore, the regenerated MWCNTs and MWCNTs-OCH$_2$CO$_2$H oxygen content decreased to 34.39 and 32.37% respectively (Fig. E4 and E5), due to the removal of oxygen containing group through decarboxylation. Generally, the data collected suggests that the decrease in adsorption capacity could be

Table 5
Thermodynamic parameters for As(V) and Mn(VII) adsorption onto MWCNTs and MWCNTs-OCH$_2$CO$_2$H.

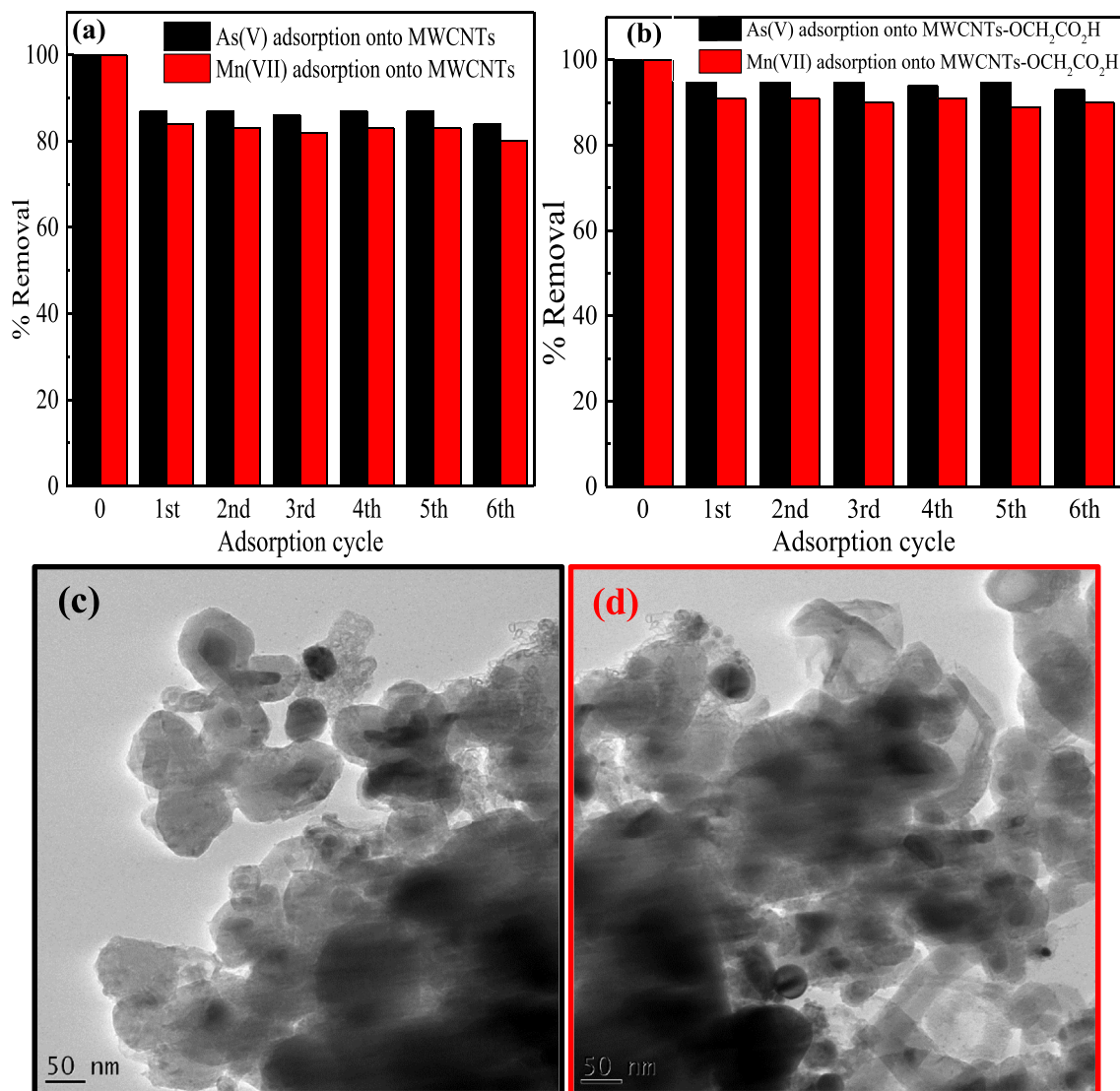| Heavy metal	T (°C)	MWCNTs			MWCNTs-OCH$_2$CO$_2$H		
		ΔG° (kJ/mol)	ΔH° (kJ/mol)	ΔS° (J/mol)	ΔG° (kJ/mol)	ΔH° (kJ/mol)	ΔS° (kJ/mol)
As(V)	25	−765.40 ± 1.00	263.46 ± 0.40	41.15 ± 0.50	−812.05 ± 1.20	194.45 ± 0.20	40.26 ± 0.40
	30	−971.17 ± 2.00			−1013.34 ± 1.40		
	35	−1382.71 ± 1.20			−1415.94 ± 2.50		
	40	−1794.25 ± 2.00			−1818.54 ± 1.60		
	50	−2205.80 ± 1.00			−2221.13 ± 2.00		
	25	−703.27 ± 2.00	494.09 ± 0.50	47.89 ± 0.60	−862.03 ± 1.50	196.72 ± 0.30	42.35 ± 0.40
	30	−942.74 ± 1.80			−1073.78 ± 2.00		
Mn(VII)	35	−1182.21 ± 1.00			−1497.28 ± 1.00		
	40	−1421.69 ± 2.00			−1920.78 ± 2.20		
	50	−1900.63 ± 1.00			−2344.27 ± 2.00		

Fig. 4. Regeneration capacity of (a) MWCNTs; (b) MWCNTs-OCH$_2$CO$_2$H for adsorption of As(V) and Mn(VII); TEM image of regenerated (c) MWCNTs and (d) MWCNTs-OCH$_2$CO$_2$H.

due to the remnant As(V) and Mn(VII) and loss of functional groups containing oxygen. The decrease in adsorption capacity was adjudged low after 6 cycles, thereby showing a remarkable reusability potential for industrial wastewater treatment. Also, the used adsorbents could be disposed after the removal of heavy metals beyond when it could no longer be regenerated. The reusability would reduce the operation cost of MWCNTs and MWCNTs-OCH$_2$CO$_2$H in water treatment, and also mitigate the discharge of MWCNTs and MWCNTs-OCH$_2$CO$_2$H into the environment.

4. Conclusion

The optimization of the synthesis parameters of Fe−Ni/AC catalyst for the growth of MWCNTs and carboxylated MWCNTs-OCH$_2$CO$_2$H and for the adsorption of As(V) and Mn(VII) from industrial wastewater were investigated. The optimum yield of 92.5% of the developed Fe−Ni/AC catalyst was obtained at the following conditions: pre-calcination temperature (115 °C), pre-calcination time (10 h), stirring speed (400 rpm) and mass of AC support (10 g). The characterization results using TGA, FTIR and HRSEM/EDS confirmed the suitability of the developed catalyst for CNTs synthesis. MWCNTs and MWCNTs-OCH$_2$CO$_2$H was synthesized, characterized and carboxylated for As(V) and Mn(VII) adsorption from wastewater. BET, FTIR, TGA, XPS, HRSEM and HRTEM confirm successful growth and grafting of carboxylic groups on the MWCNTs-OCH$_2$CO$_2$H. Parametric studies indicated optimum adsorption of As(V) and Mn(VII) occurred at contact time (60 min), adsorbent dosage (30 mg), temperature (50 °C) and pH (6) for both nano-adsorbents. The adsorption of As(V) and Mn(VII) was also found to depend on the strength of the ions and nature of the electrolytes. The adsorption isotherm and kinetic model showed good agreement with Langmuir and pseudo-second order model for both As(V) and Mn(VII) adsorption by MWCNTs and MWCNTs-OCH$_2$CO$_2$H. Carboxylation phenomena enhanced the adsorption capacity of As(V) from 200 to 250 mg/g and Mn(VII) from 192 to 238 mg/g. The thermodynamic result showed that As(V) and Mn(VII) adsorption by MWCNTs and MWCNTs-OCH$_2$CO$_2$H was endothermic, spontaneous and chemisorption by nature. The reusability capabilities of MWCNTs and MWCNTs-OCH$_2$CO$_2$H revealed that both nano-adsorbents can be recycled and re-useable after 6 cycle regeneration. Future work will include utilization of the nano-adsorbents in soil remediation of toxic heavy metals. New

insights were revealed by the results of this study for chemical functionalization of MWCNTs adsorbents and would create awareness on MWCNTs linked technologies for water, air and soil pollution.

Declaration of competing interest

The authors declared no potential conflicts of interest.

CRediT authorship contribution statement

T.C. Egbosiuba: Conceptualization, Investigation, Methodology, Data curation, Writing - original draft, Funding acquisition, Writing - review & editing. **A.S. Abdulkareem:** Supervision, Project administration, Resources, Validation. **A.S. Kovo:** Supervision, Project administration, Validation. **E.A. Afolabi:** Supervision, Project administration, Validation. **J.O. Tijani:** Formal analysis, Writing - review & editing, Software, Validation. **W.D. Roos:** Methodology, Writing - review & editing, Data curation, Formal analysis, Software.

Acknowledgements

Appendix A. Supplementary data

Supplementary data to this article can be found online at https://doi.org/10.1016/j.chemosphere.2020.126780.

References

Acomb, J.C., Wu, C., Williams, P.T., 2016. The use of different metal catalysts for the simultaneous production of carbon nanotubes and hydrogen from pyrolysis of plastic feedstocks. Appl. Catal. B Environ. 180, 497–510. https://doi.org/10.1016/j.apcatb.2015.06.054.

Ahamed, A., Veksha, A., Yin, K., Weerachanchai, P., Giannis, A., Lisak, G., 2019. Environmental impact assessment of converting flexible packaging plastic waste to pyrolysis oil and multi-walled carbon nanotubes. J. Hazard Mater. 121449 https://doi.org/10.1016/j.jhazmat.2019.121449.

Alijani, H., Shariatinia, Z., 2017. Effective aqueous arsenic removal using zero valent iron doped MWCNT synthesized by in situ CVD method using natural α-Fe2O3as a precursor. Chemosphere. Elsevier Ltd. https://doi.org/10.1016/j.chemosphere.2016.12.106.

Aliyu, A., Abdulkareem, A.S., Kovo, A.S., Abubakre, O.K., Tijani, J.O., 2017. Synthesize multi-walled carbon nanotubes via catalytic chemical vapour deposition method on fe-ni bimetallic catalyst supported on kaolin. Carbon Lett 21, 33–50. https://doi.org/10.5714/CL.2017.21.033.

Almkhelfe, H., Li, X., Thapa, P., Hohn, K.L., Amama, P.B., 2018. Carbon nanotube-supported catalysts prepared by a modified photo-Fenton process for Fischer–Tropsch synthesis. J. Catal. 361, 278–289. https://doi.org/10.1016/j.jcat.2018.02.009.

Ates, A., Akgül, G., 2015. PT SC. Powder Technol. https://doi.org/10.1016/j.powtec.2015.10.021.

Bankole, M.T., Mohammed, I.A., Abdulkareem, A.S., Tijani, J.O., Ochigbo, S.S., Abubakre, O.K., Afolabi, A.S., 2018a. Optimization of supported bimetallic (Fe-Co/CaCO3) catalyst synthesis parameters for carbon nanotubes growth using factorial experimental design. J. Alloys Compd. 749, 85–102. https://doi.org/10.1016/j.jallcom.2018.03.150.

Bankole, M.T., Mohammed, I.A., Abdulkareem, A.S., Tijani, J.O., Ochigbo, S.S., Abubakre, O.K., Afolabi, A.S., 2018b. Optimization of supported bimetallic (Fe-Co/CaCO3) catalyst synthesis parameters for carbon nanotubes growth using factorial experimental design. J. Alloys Compd. https://doi.org/10.1016/j.jallcom.2018.03.150.

Bhateria, R., Singh, R., 2019. A review on nanotechnological application of magnetic iron oxides for heavy metal removal. J. Water Process Eng. 31, 100845. https://doi.org/10.1016/j.jwpe.2019.100845.

Bora, A.J., Dutta, R.K., 2019. Removal of metals (Pb, Cd, Cu, Cr, Ni, and Co)from drinking water by oxidation-coagulation-absorption at optimized pH. J. Water Process Eng. 31, 100839. https://doi.org/10.1016/j.jwpe.2019.100839.

Byun, S.H., Chung, J.W., Kwak, S.Y., 2019. Thermally regenerable multi-functional membrane for heavy-metal detection and removal. J. Water Process Eng. 29, 100757. https://doi.org/10.1016/j.jwpe.2019.01.018.

Chen, W.Q., Veksha, A., Lisak, G., 2020. Graphene-like Carbon Nanosheets Grown over Alkali-Earth Metal Oxides: Effects of Chemical Composition and Physico-Chemical Properties, Carbon. Elsevier Ltd. https://doi.org/10.1016/j.carbon.2019.12.048.

Cheng, S., Zhang, L., Xia, H., Peng, J., Shu, J., Li, C., Jiang, X., Zhang, Q., 2017. Adsorption behavior of methylene blue onto waste-derived adsorbent and exhaust gases recycling. RSC Adv. 7, 27331–27341. https://doi.org/10.1039/c7ra01482a.

Çifçi, D.İ., Meriç, S., 2017. Manganese adsorption by iron impregnated pumice composite. Colloids Surfaces A Physicochem. Eng. Asp. 522, 279–286. https://doi.org/10.1016/j.colsurfa.2017.03.004.

Egbosiuba, T.C., Abdulkareem, A.S., Kovo, A.S., Afolabi, E.A., Tijani, J.O., Auta, M., Roos, W.D., 2019. Ultrasonic enhanced adsorption of methylene blue onto the optimized surface area of activated carbon: adsorption isotherm, kinetics and thermodynamics. Chem. Eng. Res. Des. https://doi.org/10.1016/j.cherd.2019.10.016.

Fathy, N.A., 2017. Carbon nanotubes synthesis using carbonization of pretreated rice straw through chemical vapor deposition of camphor. RSC Adv. 7, 28535–28541. https://doi.org/10.1039/c7ra04882c.

Fu, W., Chen, H., Yang, S., Huang, W., Huang, Z., 2019. Poly(-diallyldimethylammonium-MoS4) based amorphous molybdenum sulphide composite for selectively mercury uptake from wastewater across a large pH region. Chemosphere 232, 9–17. https://doi.org/10.1016/j.chemosphere.2019.05.182.

Gholipour, A., Zahabi, H., Stefanakis, A.I., 2020. Chemosphere A novel pilot and full-scale constructed wetland study for glass industry wastewater treatment. Chemosphere 247, 125966. https://doi.org/10.1016/j.chemosphere.2020.125966.

Ho, Y.S., 2006. Second-order kinetic model for the sorption of cadmium onto tree fern: a comparison of linear and non-linear methods. Water Res. 40, 119–125. https://doi.org/10.1016/j.watres.2005.10.040.

Huang, J., Huang, Z.L., Zhou, J.X., Li, C.Z., Yang, Z.H., Ruan, M., Li, H., Zhang, X., Wu, Z.J., Qin, X.L., Hu, J.H., Zhou, K., 2019. Enhancement of heavy metals removal by microbial flocculant produced by Paenibacillus polymyxa combined with an insufficient hydroxide precipitation. Chem. Eng. J. 374, 880–894. https://doi.org/10.1016/j.cej.2019.06.009.

Jia, J., Veksha, A., Lim, T.T., Lisak, G., 2020. In situ grown metallic nickel from X–Ni (X=La, Mg, Sr) oxides for converting plastics into carbon nanotubes: influence of metal–support interaction. J. Clean. Prod. 258 https://doi.org/10.1016/j.jclepro.2020.120633.

Jiang, J., Lu, S., Wang, W.K., Huang, G.X., Huang, B.C., Zhang, F., Zhang, Y.J., Yu, H.Q., 2018. Ultrahigh electrocatalytic oxygen evolution by iron-nickel sulfide nanosheets/reduced graphene oxide nanohybrids with an optimized autoxidation process. Nanomater. Energy 43, 300–309. https://doi.org/10.1016/j.nanoen.2017.11.049.

Jiang, L., Li, S., Yu, H., Zou, Z., Hou, X., Shen, F., Li, C., Yao, X., 2016. Amino and thiol modified magnetic multi-walled carbon nanotubes for the simultaneous removal of lead, zinc, and phenol from aqueous solutions. Appl. Surf. Sci. 369, 398–413. https://doi.org/10.1016/j.apsusc.2016.02.067.

Joseph, L., Jun, B.M., Flora, J.R.V., Park, C.M., Yoon, Y., 2019. Removal of heavy metals from water sources in the developing world using low-cost materials: a review. Chemosphere 229, 142–159. https://doi.org/10.1016/j.chemosphere.2019.04.198.

Jun, B.M., Kim, S., Kim, Y., Her, N., Heo, J., Han, J., Jang, M., Park, C.M., Yoon, Y., 2019. Comprehensive evaluation on removal of lead by graphene oxide and metal organic framework. Chemosphere 231, 82–92. https://doi.org/10.1016/j.chemosphere.2019.05.076.

Jun, L.Y., Mubarak, N.M., Yon, L.S., Bing, C.H., Khalid, M., Abdullah, E.C., 2018. Comparative study of acid functionization of carbon nanotube via ultrasonic and reflux mechanism. J. Environ. Chem. Eng. 6, 5889–5896. https://doi.org/10.1016/j.jece.2018.09.008.

Kang, J., Duan, X., Wang, C., Sun, H., Tan, X., Tade, M.O., Wang, S., 2018. Nitrogen-doped bamboo-like carbon nanotubes with Ni encapsulation for persulfate activation to remove emerging contaminants with excellent catalytic stability. Chem. Eng. J. 332, 398–408. https://doi.org/10.1016/j.cej.2017.09.102.

Kazak, O., Eker, Y.R., Bingol, H., Tor, A., 2018. Preparation of chemically-activated high surface area carbon from waste vinasse and its efficiency as adsorbent material. J. Mol. Liq. 272, 189–197. https://doi.org/10.1016/j.molliq.2018.09.085.

Langmuir, I., 1918. The adsorption of gases on plane surfaces of glass, mica and platinum. J. Am. Chem. Soc. 40, 1361–1403. https://doi.org/10.1021/ja02242a004.

Lee, C.G., Lee, S., Park, J.A., Park, C., Lee, S.J., Kim, S.B., An, B., Yun, S.T., Lee, S.H., Choi, J.W., 2017. Removal of copper, nickel and chromium mixtures from metal plating wastewater by adsorption with modified carbon foam. Chemosphere 166, 203–211. https://doi.org/10.1016/j.chemosphere.2016.09.093.

Lima, H.H.C., Maniezzo, R.S., Llop, M.E.G., Kupfer, V.L., Arroyo, P.A., Guilherme, M.R., Rubira, A.F., Girotto, E.M., Rinaldi, A.W., 2019. Synthesis and characterization of

pecan nutshell-based adsorbent with high specific area and high methylene blue adsorption capacity. J. Mol. Liq. 276, 570—576. https://doi.org/10.1016/j.molliq.2018.12.010.

Liu, D., Deng, S., Maimaiti, A., Wang, B., Huang, J., Wang, Y., Yu, G., 2018. As(III) and As(V) adsorption on nanocomposite of hydrated zirconium oxide coated carbon nanotubes. J. Colloid Interface Sci. 511, 277—284. https://doi.org/10.1016/j.jcis.2017.10.004.

Luo, L., Qin, X., Wu, J., Liang, G., Li, Q., Liu, M., Kang, F., Chen, G., Li, B., 2018. An interwoven MoO3@CNT scaffold interlayer for high-performance lithium-sulfur batteries. J. Mater. Chem. 6, 8612—8619. https://doi.org/10.1039/c8ta01726c.

Maharjan, M., Wai, N., Veksha, A., Giannis, A., Lim, T.M., Lisak, G., 2019. Sal wood sawdust derived highly mesoporous carbon as prospective electrode material for vanadium redox flow batteries. J. Electroanal. Chem. 834, 94—100. https://doi.org/10.1016/j.jelechem.2018.12.049.

Mahmoud, M.E., El-said, G.F., Rashedy, I.R.K., Abdelfattah, A.M., 2019. Assembly and Implementation of an Eco-Friendly Marine Nanosediment for Adsorptive Removal of Heptavalent Manganese: Adsorption Isotherm, Thermodynamic and Kinetics Studies. Powder Technology. Elsevier B.V. https://doi.org/10.1016/j.powtec.2019.09.063.

Malekimoghadam, R., 2018. 3 — Carbon Nanotubes Processing, Carbon Nanotube-Reinforced Polymers. Elsevier Inc. https://doi.org/10.1016/B978-0-323-48221-9.00003-0.

Martinez—Vargas, S., Martínez, A.I., Hernández—Beteta, E.E., Mijangos—Ricardez, O.F., Vázquez—Hipólito, V., Patiño-Carachure, C., López—Luna, J., 2018. As(III) and As(V) adsorption on manganese ferrite nano-particles. J. Mol. Struct. 1154, 524—534. https://doi.org/10.1016/j.molstruc.2017.10.076.

Moo, J.G.S., Veksha, A., Oh, W. Da, Giannis, A., Udayanga, W.D.C., Lin, S.X., Ge, L., Lisak, G., 2019. Plastic derived carbon nanotubes for electrocatalytic oxygen reduction reaction: effects of plastic feedstock and synthesis temperature. Electrochem. Commun. 101, 11—18. https://doi.org/10.1016/j.elecom.2019.02.014.

Mouni, L., Belkhiri, L., Bollinger, J.C., Bouzaza, A., Assadi, A., Tirri, A., Dahmoune, F., Madani, K., Remini, H., 2018. Removal of Methylene Blue from aqueous solutions by adsorption on Kaolin: kinetic and equilibrium studies. Appl. Clay Sci. 153, 38—45. https://doi.org/10.1016/j.clay.2017.11.034.

Nadar, A., Banerjee, A.M., Pai, M.R., Pai, R.V., Meena, S.S., Tewari, R., Tripathi, A.K., 2018. Catalytic properties of dispersed iron oxides Fe2O3/MO2 (M = Zr, Ce, Ti and Si) for sulfuric acid decomposition reaction: role of support. Int. J. Hydrogen Energy 43, 37—52. https://doi.org/10.1016/j.ijhydene.2017.10.163.

Nahil, M.A., Wu, C., Williams, P.T., 2015. Influence of metal addition to Ni-based catalysts for the co-production of carbon nanotubes and hydrogen from the thermal processing of waste polypropylene. Fuel Process. Technol. 130, 46—53. https://doi.org/10.1016/j.fuproc.2014.09.022.

Oh, W. Da, Lee, M.G.H., Chanaka Udayanga, W.D., Veksha, A., Bao, Y., Giannis, A., Lim, J.W., Lisak, G., 2019. Insights into the single and binary adsorption of copper(II) and nickel(II) on hexagonal boron nitride: performance and mechanistic studies. J. Environ. Chem. Eng. 7, 102872. https://doi.org/10.1016/j.jece.2018.102872.

Oh, W. Da, Wong, Z., Chen, X., Lin, K.Y.A., Veksha, A., Lisak, G., He, C., Lim, T.T., 2020. Enhanced activation of peroxydisulfate by CuO decorated on hexagonal boron nitride for bisphenol A removal. Chem. Eng. J. 393, 124714. https://doi.org/10.1016/j.cej.2020.124714.

Pathan, S., Pandita, N., Kishore, N., 2016. Acid functionalized-nanoporous carbon/MnO2 composite for removal of arsenic from aqueous medium. Arab. J. Chem. https://doi.org/10.1016/j.arabjc.2016.12.011.

Pérez-Mayoral, E., Calvino-Casilda, V., Soriano, E., 2016. Metal-supported carbon-based materials: opportunities and challenges in the synthesis of valuable products. Catal. Sci. Technol. 6, 1265—1291. https://doi.org/10.1039/c5cy01437a.

Pietrelli, L., Ippolito, N.M., Ferro, S., Dovì, V.G., Vocciante, M., 2019. Removal of Mn and as from drinking water by red mud and pyrolusite. J. Environ. Manag. 237, 526—533. https://doi.org/10.1016/j.jenvman.2019.02.093.

Roh, J.S., Park, J.S., Roh, J.M., Park, H.B., Do, S.H., 2018. The pretreatment of granular activated carbon using sodium persulfate and hydrogen peroxide under basic conditions: properties, metal impregnation, and As(V) adsorption. Mater. Chem. Phys. 218, 317—325. https://doi.org/10.1016/j.matchemphys.2018.07.045.

Sankararamakrishnan, N., Gupta, A., Vidyarthi, S.R., 2014. Enhanced arsenic removal at neutral pH using functionalized multiwalled carbon nanotubes. J. Environ. Chem. Eng. 2, 802—810. https://doi.org/10.1016/j.jece.2014.02.010.

Shukrullah, S., Mohamed, N.M., Shaharun, M.S., Naz, M.Y., 2016. Parametric study on vapor-solid-solid growth mechanism of multiwalled carbon nanotubes. Mater. Chem. Phys. 176, 32—43. https://doi.org/10.1016/j.matchemphys.2016.03.013.

Siddiqui, S.I., Chaudhry, S.A., 2017. Iron oxide and its modified forms as an adsorbent for arsenic removal: a comprehensive recent advancement. Process Saf. Environ. Protect. 111, 592—626. https://doi.org/10.1016/j.psep.2017.08.009.

Siddiqui, S.I., Naushad, M., Chaudhry, S.A., 2019. Promising prospects of nano-materials for arsenic water remediation: a comprehensive review. Process Saf. Environ. Protect. 60—97. https://doi.org/10.1016/j.psep.2019.03.037.

Sivakumar, V.M., Abdullah, A.Z., Mohamed, A.R., Chai, S.P., 2011. Optimized parameters for carbon nanotubes synthesis over Fe and Ni catalysts VIA methane CVD. Rev. Adv. Mater. Sci. 27, 25—30.

Siyal, A.A., Shamsuddin, M.R., Rabat, N.E., Zulfiqar, M., Man, Z., Low, A., 2019. Fly ash based geopolymer for the adsorption of anionic surfactant from aqueous solution. J. Clean. Prod. 229, 232—243. https://doi.org/10.1016/j.jclepro.2019.04.384.

Su, H., Ye, Z., Hmidi, N., 2017. High-performance iron oxide—graphene oxide nanocomposite adsorbents for arsenic removal. Colloids Surfaces A Physicochem. Eng. Asp. 522, 161—172. https://doi.org/10.1016/j.colsurfa.2017.02.065.

US EPA, 2012. US Environmental Protection Agency: 2012 Edition of the Drinking Water Standards and Health Advisories, vol. 2012. Drink. Water Stand. Heal. Advis. 2—6, https://doi.org/EPA 822-S-12-001.

Veksha, A., Yin, K., Moo, J.G.S., Oh, W. Da, Ahamed, A., Chen, W.Q., Weerachanchai, P., Giannis, A., Lisak, G., 2020. Processing of flexible plastic packaging waste into pyrolysis oil and multi-walled carbon nanotubes for electrocatalytic oxygen reduction. Journal of Hazardous Materials. Elsevier B.V. https://doi.org/10.1016/j.jhazmat.2019.121256.

Who, 2017. Guidelines for Drinking-Water Quality. https://doi.org/10.1016/S1462-0758(00)00006-6. Fourth Ed. 631.

Wu, L.K., Wu, H., Zhang, H. Bin, Cao, H.Z., Hou, G.Y., Tang, Y.P., Zheng, G.Q., 2018. Graphene oxide/CuFe 2 O 4 foam as an efficient absorbent for arsenic removal from water. Chem. Eng. J. 334, 1808—1819. https://doi.org/10.1016/j.cej.2017.11.096.

Wu, W., Lin, F., Yang, X., Wang, B., Lu, X., Chen, Q., Ye, F., Zhao, S., 2020. Facile synthesis of magnetic carbon nanotubes derived from ZIF-67 and application to magnetic solid-phase extraction of profens from human serum. Talanta 207, 120284. https://doi.org/10.1016/j.talanta.2019.120284.

Xu, J., Cao, Z., Zhang, Y., Yuan, Z., Lou, Z., Xu, X., Wang, X., 2018. A review of functionalized carbon nanotubes and graphene for heavy metal adsorption from water: preparation, application, and mechanism. Chemosphere 195, 351—364. https://doi.org/10.1016/j.chemosphere.2017.12.061.

Yadav, M.D., Dasgupta, K., Patwardhan, A.W., Kaushal, A., Joshi, J.B., 2019. Kinetic study of single-walled carbon nanotube synthesis by thermocatalytic decomposition of methane using floating catalyst chemical vapour deposition. Chem. Eng. Sci. 91—103. https://doi.org/10.1016/j.ces.2018.10.050.

Yang, K., Liu, Y., Li, Y., Cao, Z., Zhou, C., Wang, Z., Zhou, X., Baig, S.A., Xu, X., 2019a. Applications and characteristics of Fe-Mn binary oxides for Sb(V) removal in textile wastewater: selective adsorption and the fixed-bed column study. Chemosphere 232, 254—263. https://doi.org/10.1016/j.chemosphere.2019.05.194.

Yang, K., Lou, Z., Fu, R., Zhou, J., Xu, J., Baig, S.A., Xu, X., 2018. Multiwalled carbon nanotubes incorporated with or without amino groups for aqueous Pb(II) removal: comparison and mechanism study. J. Mol. Liq. 260, 149—158. https://doi.org/10.1016/j.molliq.2018.03.082.

Yang, Y., Zhang, H., Yan, Y., 2019b. Synthesis of CNTs on stainless steel microfibrous composite by CVD: effect of synthesis condition on carbon nanotube growth and structure. Compos. B Eng. 160, 369—383. https://doi.org/10.1016/j.compositesb.2018.12.100.

Yao, D., Zhang, Y., Williams, P.T., Yang, H., Chen, H., 2018. Co-production of hydrogen and carbon nanotubes from real-world waste plastics: influence of catalyst composition and operational parameters. Appl. Catal. B Environ. 221, 584—597. https://doi.org/10.1016/j.apcatb.2017.09.035.

Yatom, S., Selinsky, R.S., Koel, B.E., Raitses, Y., 2017. "Synthesis-on" and "synthesis-off" modes of carbon arc operation during synthesis of carbon nanotubes. Carbon N. Y. 125, 336—343. https://doi.org/10.1016/j.carbon.2017.09.034.

Zhao, C., Ge, R., Zhen, Y., Wang, Y., Li, Z., Shi, Y., Chen, X., 2019a. A hybrid process of coprecipitation-induced crystallization-capacitive deionization-ion exchange process for heavy metals removal from hypersaline ternary precursor wastewater. Chem. Eng. J. 378, 122136. https://doi.org/10.1016/j.cej.2019.122136.

Zhao, L., Chen, J., Xiong, N., Bai, Y., Yilihamu, A., Ma, Q., Yang, S., Wu, D., Yang, S.T., 2019b. Carboxylation as an effective approach to improve the adsorption performance of graphene materials for Cu2+ removal. Sci. Total Environ. 682, 591—600. https://doi.org/10.1016/j.scitotenv.2019.05.190.

Zheng, N., Sun, W., Liu, H.Y., Huang, Y., Gao, J., Mai, Y.W., 2018. Effects of carboxylated carbon nanotubes on the phase separation behaviour and fracture-mechanical properties of an epoxy/polysulfone blend. Compos. Sci. Technol. 159, 180—188. https://doi.org/10.1016/j.compscitech.2018.02.039.